

Light Element Discontinuities Suggest an Early Termination of Star Formation in the Globular Cluster NGC 6402 (M14)

Christian I. Johnson,¹[★] Nelson Caldwell,¹ R. Michael Rich,² Mario Mateo,³ and John I. Bailey, III⁴

¹*Center for Astrophysics | Harvard & Smithsonian, 60 Garden Street, Cambridge, MA 02138, USA*

²*Department of Physics and Astronomy, UCLA, 430 Portola Plaza, Box 951547, Los Angeles, CA 90095-1547, USA*

³*Department of Astronomy, University of Michigan, Ann Arbor, MI 48109, USA*

⁴*Department of Physics, UCSB, Santa Barbara, CA 93016, USA*

Accepted XXX. Received YYY; in original form ZZZ

ABSTRACT

NGC 6402 is among the most massive globular clusters in the Galaxy, but little is known about its detailed chemical composition. Therefore, we obtained radial velocities and/or chemical abundances of 11 elements for 41 red giant branch cluster members using high resolution spectra obtained with the Magellan-M2FS instrument. We find NGC 6402 to be only moderately metal-poor with $\langle[\text{Fe}/\text{H}]\rangle = -1.13$ dex ($\sigma = 0.05$ dex) and to have a mean heliocentric radial velocity of -61.1 km s⁻¹ ($\sigma = 8.5$ km s⁻¹). In general, NGC 6402 exhibits mean composition properties that are similar to other inner Galaxy clusters, such as $[\alpha/\text{Fe}] \sim +0.3$ dex, $[\text{Cr}, \text{Ni}/\text{Fe}] \sim 0.0$ dex, and $\langle[\text{La}/\text{Eu}]\rangle = -0.08$ dex. Similarly, we find large star-to-star abundance variations for O, Na, Mg, Al, and Si that are indicative of gas that experienced high temperature proton-capture burning. Interestingly, we detect three distinct populations, but also find large gaps in the $[\text{O}/\text{Fe}]$, $[\text{Na}/\text{Fe}]$, and $[\text{Al}/\text{Fe}]$ distributions that may provide the first direct evidence of delayed formation for intermediate composition stars. A qualitative enrichment model is discussed where clusters form stars through an early ($\lesssim 5\text{--}10$ Myr) phase, which results in first generation and “extreme” composition stars, and a delayed phase ($\gtrsim 40$ Myr), which results in the dilution of processed and pristine gas and the formation of intermediate composition stars. For NGC 6402, the missing intermediate composition stars suggest the delayed phase terminated prematurely, and as a result the cluster may uniquely preserve details of the chemical enrichment process.

Key words: galaxies: star clusters: individual: NGC 6402 (M14)

1 INTRODUCTION

Early high resolution spectroscopic work on Galactic globular clusters discovered the presence of large, often correlated, star-to-star abundance variations for elements ranging from at least carbon through aluminum (e.g., see reviews by Kraft 1994; Gratton et al. 2004, and references therein). The observed patterns, such as C-N, O-Na, and Mg-Al anti-correlations coupled with Na-Al correlations, hinted at an origin rooted in high temperature (> 40 MK) proton-capture nucleosynthesis (e.g., Denisenkov & Denisenkova 1990; Langer et al. 1993). Although originally observed in bright red giant branch (RGB) stars in some of the nearest

and most massive clusters, recent large sample spectroscopic surveys (e.g., Carretta et al. 2009a,b) have shown that (anti-)correlated light element abundance variations are ubiquitous patterns found in nearly all old globular clusters and at all evolutionary stages (e.g., Gratton et al. 2001).

Interestingly, the abundance variations tend to “clump” into discrete groups rather than trace a composition continuum. The data indicate that most old globular clusters are not monolithic populations, and instead are collections of two or more chemically distinct groups. The discrete nature of globular cluster formation and enrichment is most clearly seen in the *Hubble Space Telescope* (HST) color-magnitude diagram (CMD) compilations of Piotto et al. (2015) and Milone et al. (2017), but is also visible in the light element abundance diagrams of some spectroscopic

[★] E-mail: cjohnson@cfa.harvard.edu

analyses (e.g., Carretta et al. 2012; Cohen & Kirby 2012; Mucciarelli et al. 2015; Johnson et al. 2017c; Marino et al. 2017; Carretta et al. 2018).

With few exceptions¹, globular clusters can be broadly decomposed into sets of “first generation” and “second generation” stars. The first generation stars are characterized as having light element compositions that mirror those of similar metallicity halo field stars (e.g., Sneden et al. 2004) while the second generation groups tend to have lower C, O, and Mg abundances and higher He, N, Na, and Al abundances. Aside from a general consensus that second generation stars likely formed from gas that was processed at temperatures exceeding 40–80 MK (e.g., Langer et al. 1993; Prantzos et al. 2007; Denissenkov et al. 2015; Ventura et al. 2018), little agreement exists regarding the origins of the (anti-)correlated light element variations. Various enrichment sites have been proposed, including intermediate mass asymptotic giant branch (AGB) stars (e.g., Ventura & D’Antona 2009; Karakas et al. 2014), fast rotating massive stars (e.g., Decressin et al. 2007; Krause et al. 2013), interacting massive binary stars (de Mink et al. 2009; Bastian et al. 2013), Wolf-Rayet stars (Smith 2006), white dwarf novae (Maccarone & Zurek 2012), black hole accretion disks (Breen 2018), and supermassive stars (Denissenkov & Hartwick 2014). However, these scenarios currently fail to simultaneously explain all globular cluster composition characteristics (e.g., Bastian et al. 2015; Renzini et al. 2015; Bastian & Lardo 2018).

Despite the theoretical difficulties in explaining the star-to-star abundance variations, observations clearly show strong links between a cluster’s horizontal branch (HB) extension, cluster mass, and composition range. In particular, clusters possessing warmer blue HB populations and larger present-day masses tend to exhibit more extreme [O/Na] and [Mg/Al] abundance ranges (Carretta et al. 2007, 2010a; Gratton et al. 2010). A significant fraction of clusters with $M_V \lesssim -8$ exhibit variations in Fe-peak and s-process abundances as well, and some evidence indicates that many of these “Fe-complex” or “Type II” clusters may be the remnant cores of former dwarf galaxies (e.g., Da Costa 2016; Johnson et al. 2017a; Marino et al. 2018). In fact, Lee et al. (2007) suggests that most or all clusters with significant blue HB populations have an accretion origin.

Following the evidence outlined above, we targeted RGB stars in the massive blue HB inner Galaxy cluster NGC 6402 for analysis with high resolution spectroscopy. Although little is known about the cluster’s detailed chemical composition, several lines of evidence, including possible membership in a stellar stream (Gao et al. 2007), suggest NGC 6402 may be an accreted system. For instance, NGC 6402 contains a rare CH star (Côté et al. 1997). Such objects are common in dwarf galaxies (e.g., Cannon et al. 1981), but in the Milky Way only two other clusters, ω Cen (Harding 1962; Dickens 1972; Bond 1975) and NGC 6426 (Sharina et al. 2012), have confirmed detections. Additionally, Contreras Peña et al. (2018) found that NGC 6402 is

likely an Oosterhoff-intermediate cluster, which is a signature more reminiscent of local dwarf galaxies than Galactic globular clusters.

NGC 6402 is among the brightest globular clusters in the Milky Way, and nearly all of the clusters with similar luminosity possess complex chemical patterns. For example, ω Cen (e.g., Johnson & Pilachowski 2010; Marino et al. 2011a), NGC 6273 (Johnson et al. 2015, 2017b), and M 2 (Yong et al. 2014b; Milone et al. 2015a; Lardo et al. 2016) each host at least 2–3 groups of stars with distinct light and heavy element compositions, M 54 exhibits a broad metallicity distribution and may be the nuclear core of the Sagittarius dwarf galaxy (e.g., Carretta et al. 2010c), NGC 6388 and NGC 6441 have unusually extended blue HBs and light element variations for their high metallicities (e.g., Carretta & Bragaglia 2018; Gratton et al. 2007; Tailo et al. 2017), and NGC 2419 and NGC 2808 show signatures of extremely high temperature (> 100 MK) proton-capture burning (e.g., Cohen & Kirby 2012; Ventura et al. 2012; Carretta 2015; Mucciarelli et al. 2015; Prantzos et al. 2017). Although the present work does not find evidence supporting a metallicity spread, we report that NGC 6402 maintains the aforementioned trend of massive clusters exhibiting peculiar composition characteristics.

2 OBSERVATIONS AND DATA REDUCTION

The spectra for this project were obtained using the Michigan-Magellan Fiber System (M2FS; Mateo et al. 2012) and MSpec spectrograph on the Magellan-Clay 6.5m telescope at Las Campanas Observatory. Both spectrographs were configured to use the 125 μ m slits, a four amplifier slow readout mode, 1×2 binning in the dispersion and spatial directions, the “Bulge_GC1” order blocking filters, and the echelle gratings. This setup permits up to 48 fibers to be placed on targets within the 29.2’ field-of-view and produces spectra with a mean resolving power of $R \equiv \lambda/\Delta\lambda \approx 27,000$. The total wavelength coverage of all six orders ranged from ~ 6140 – 6720 Å.

A total of 42 fibers were placed on possible RGB stars within a radius of $\sim 3.6'$ from the core of NGC 6402, and an additional 6 fibers were placed on blank sky regions. No targets were selected within $0.5'$ of the cluster core due to severe crowding restricting the placement of single stars within the 1.2’’ fibers. Targets and coordinates were obtained using the Two Micron All Sky Survey (2MASS; Skrutskie et al. 2006), and membership probabilities were estimated using a fiducial sequence derived from 2MASS CMDs that only included stars within $1'$ of the cluster core. The final target selection is illustrated in Fig. 1 and spans $K_S = 9.7$ – 11.3 mag., which is equivalent to $V = 14.7$ – 15.7 mag. The brightest RGB-tip stars were not included in order to avoid targets with effective temperatures (T_{eff}) lower than ~ 4100 K. The target identifiers, J2000 coordinates, and 2MASS photometry are provided in Table 1.

The spectra were obtained under clear but moderately humid conditions with reasonable seeing ($\sim 1.2''$) on 2017 September 11, 12, and 15. The integration time totaled 18,000 seconds (5 hours) and was distributed over ten 1800 second exposures. Signal-to-noise ratios (S/N) for individual exposures were approximately 25–50 per reduced pixel.

¹ The low mass Galactic globular clusters Rup 106 and E 3 may contain only single populations of first generation stars (Villanova et al. 2013; Salinas & Strader 2015; Dotter et al. 2018).

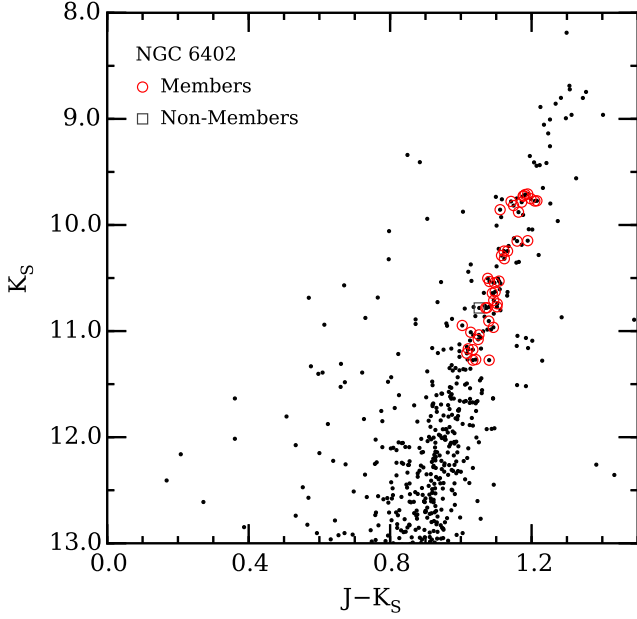


Figure 1. A 2MASS color-magnitude diagram is shown for a region within $5'$ of NGC 6402 (small black circles). Cluster member and non-member stars are indicated with open red circles and open grey boxes, respectively.

Data reduction followed the recipe outlined in Johnson et al. (2015), which primarily exploits the *dohydra* routine from IRAF² to carry out aperture identification and tracing, flat-fielding, scattered light removal, wavelength calibration, cosmic-ray removal, throughput correction, and spectrum extraction. Basic image preparation such as over-scan and bias correction, over-scan trimming, and dark current removal was completed with IRAF before processing with *dohydra*. The extracted sky spectra for each order and exposure were median combined separately and subtracted from the object spectra. The sky subtracted stellar spectra were continuum normalized, divided by a previously obtained telluric spectrum, corrected for heliocentric velocity variations, and median combined. The final S/N ranged from ~ 75 – 130 per reduced pixel.

3 RADIAL VELOCITIES AND CLUSTER MEMBERSHIP

Radial velocities were measured for each order and exposure of every star using the XCSAO cross-correlation routine (Kurtz & Mink 1998). The velocities were measured relative to a synthetic spectrum library spanning the temperature, gravity, and metallicity regime probed here. All template spectra were smoothed and resampled to match the observations. Heliocentric radial velocity corrections were calculated for each exposure using the IRAF *rvcor* routine and applied to the relative velocity measurements output from XCSAO. The mean heliocentric corrected velocities for all stars are

² IRAF is distributed by the National Optical Astronomy Observatory, which is operated by the Association of Universities for Research in Astronomy, Inc., under cooperative agreement with the National Science Foundation.

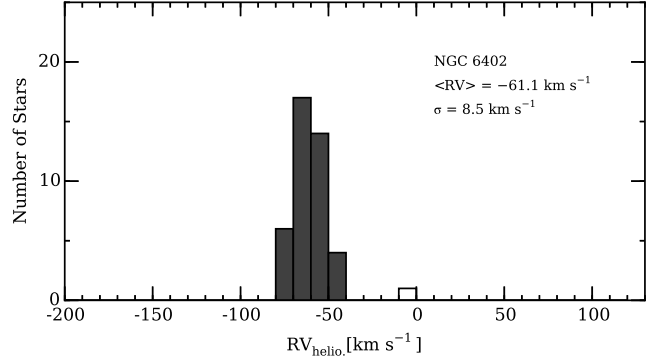


Figure 2. The heliocentric radial velocity distributions of the member (filled grey histogram) and non-member (white histogram) stars are shown using a bin width of 10 km s^{-1} .

reported in Table 1. Note that the velocity errors provided in Table 1 represent the standard deviations of all measurements (i.e., each order and exposure) and range from 0.1 – 2.0 km s^{-1} .

Fig. 2 shows the heliocentric radial velocity distribution of our targets, and indicates that the cluster members are clearly separated from the field star population. In fact, 41/42 stars observed for this program are cluster members based on velocity. The sole non-member resides at -7.7 km s^{-1} , which is consistent with the broad field distribution that peaks near -20 km s^{-1} , as noted by Côté et al. (1997). Ignoring the non-member star, we find NGC 6402 to have a mean heliocentric radial velocity of -61.1 km s^{-1} with a dispersion of 8.5 km s^{-1} . Early estimates of the cluster velocity by Webbink (1981) and Hesser et al. (1986) found values of -123 km s^{-1} and -25 km s^{-1} , respectively, but as pointed out by Côté et al. (1997) these results likely suffered from field star contamination and/or inaccurate measurements. More recent velocity estimates from Côté et al. (1997), Kimmig et al. (2015), and Baumgardt & Hilker (2018) range from -59.5 km s^{-1} to -60.7 km s^{-1} with dispersion values of 8.5 – 11.7 km s^{-1} , which are consistent with the measurements presented here.

4 DATA ANALYSIS

4.1 Stellar Atmosphere Parameters

Initial values for T_{eff} and surface gravity ($\log(g)$) were determined using the 2MASS photometry given in Table 1, the differential reddening map provided by Contreras Peña et al. (2013), the González Hernández & Bonifacio (2009) color-temperature relation, a distance of 9.5 kpc (Contreras Peña et al. 2018), $[\text{Fe}/\text{H}] = -1.2$ (Contreras Peña et al. 2018), and the K_S -band bolometric correction relation from Buzzoni et al. (2010). However, the final T_{eff} and $\log(g)$ values were set by enforcing excitation equilibrium with FeI and ionization equilibrium with FeI and FeII. Microturbulence (ξ_{mic}) was determined by removing trends in plots of $\log \epsilon(\text{FeI})$ versus line strength. Additionally, the model metallicity was set to the mean of $[\text{FeI}/\text{H}]$ and $[\text{FeII}/\text{H}]$. For each iteration, we

interpolated within the ATLAS9 grid³ of α -enhanced model atmospheres (Castelli & Kurucz 2004), and all four parameters were modified simultaneously until a satisfactory solution was achieved. Convergence failed for 6/41 members (see Table 1) and these objects were omitted from further analysis. The adopted model atmosphere parameters for all other stars, except for the lone non-member, are provided in Table 1.

A comparison of the adopted spectroscopic temperatures and those derived via photometry, assuming the recommended mean $E(B-V) = 0.57$ from Contreras Peña et al. (2013), indicated that the photometric temperatures were ~ 185 K warmer ($\sigma = 89$ K), on average. Agreement between the spectroscopic and photometric temperatures was found when the mean $E(B-V)$ was set at 0.44, which is within the range of values estimated by previous authors (see the discussion in Section 3.1 of Contreras Peña et al. 2013). The 85 K dispersion between the spectroscopic and photometric T_{eff} estimates is also equivalent to the 94 K calibration uncertainty reported by González Hernández & Bonifacio (2009) for J-Ks.

4.2 Equivalent Width and Spectrum Synthesis Analyses

The equivalent widths (EWs) and abundances of FeI, FeII, NaI, SiI, CaI, CrI, and NiI were determined using a combination of the Gaussian line profile deblender developed for Johnson et al. (2014) and the *abfind* driver of the local thermodynamic equilibrium (LTE) line analysis code MOOG⁴ (2014 version; Sneden 1973). The line list, atomic parameters, and reference solar abundances were the same as those provided in Table 2 of Johnson et al. (2015). In general, we omitted lines with $\log(\frac{EW}{\lambda}) \gtrsim -4.5$ in order to avoid strongly saturated features. A list of the final abundances derived from the EW analyses is provided in Table 2.

For the other elements presented in Table 2, namely OI, MgI, AlI, LaII, and EuII, various issues precluded the use of EW measurements and we opted to derive abundances via spectrum synthesis. Specifically, we used the MOOG *synth* driver along with line lists from Johnson et al. (2014) for O, Johnson et al. (2015) for Mg and Al, Lawler et al. (2001a) for La, and Lawler et al. (2001b) for Eu. The reference solar abundances are the same as those in Johnson et al. (2014) for O and Johnson et al. (2015) for the remaining elements derived from spectrum synthesis.

Since O abundances are sensitive to the total CNO composition, we determined $\log \epsilon(\text{OI})$ using an iterative process of fitting the 6300 Å [OI] feature and several CN bands throughout the spectra. In all syntheses, we held the [C/Fe] ratio fixed at -0.3 dex and varied the [O/Fe] and [N/Fe] ratios until a satisfactory fit was obtained for both the O and CN features. The 6300 Å [OI] line is also blended with NiI, which we accounted for by setting the [Ni/Fe] ratio to match the value determined from the EW analysis. The 6696/6698 Å AlI lines are also moderately blended with CN and were only fit after determining the relative CNO abundances.

The 6318/6319 Å MgI lines used here are relatively weak, moderately blended, and can be significantly affected by a shallow but broad CaI autoionization feature. The impact of the autoionization feature was gauged by examining the continuum suppression between 6316 and 6320 Å, and when necessary the strength of the autoionization feature was modified by changing the Ca abundance in the synthesis. Although the impact of the autoionization feature was not too severe in the observed stars, the blending and weak line strengths of the 6318/6319 Å triplet limited the accuracy of our [Mg/Fe] measurements. As a result, [Mg/Fe] is likely the most poorly constrained measurement presented here.

The LaII and EuII lines used here are moderately weak ($EW \lesssim 50\text{m}\text{\AA}$) but can be affected by hyperfine broadening, isotope shifts, or both (in the case of Eu). For La, the 6262 Å line is the broadest feature but also the most reliably fit with the Lawler et al. (2001a) line list. Therefore, most of the La abundances presented in Table 2 rely on this feature. Similarly, the 6645 Å line was the most reliably available feature for Eu. In all syntheses, we adopted the solar ^{151}Eu and ^{153}Eu ratios presented in Lawler et al. (2001b).

4.3 Abundance Uncertainties

As noted in Section 2 and demonstrated in Fig. 3, the high S/N of the M2FS data used in this project suggest that the absolute abundance uncertainties are dominated by deficiencies in how radiative transfer is calculated and model atmospheres constructed rather than pure measurement errors. However, since the stars utilized in this study span a small range in temperature, surface gravity, and metallicity, the relative uncertainty due to changes in the model atmosphere parameters is likely the dominant error source.

We determined the abundance uncertainties relative to changes in the model atmosphere parameters following the methods outlined in Johnson et al. (2018). Specifically, we individually adjusted T_{eff} , $\log(g)$, [Fe/H], and ξ_{mic} by 85 K, 0.15 cgs, 0.10 dex, and 0.10 km s^{-1} , respectively, while holding the other parameters fixed and redetermined the abundances of each element. The ΔT_{eff} value was chosen based on the standard deviation of the differences between spectroscopic and photometric temperatures (see Section 4.1) while the $\Delta \log(g)$ uncertainty was estimated as the mean dispersion in the spectroscopic surface gravity when stars were partitioned by T_{eff} into 100 K groups. Similarly, the $\Delta[\text{Fe}/\text{H}]$ value was based on the mean line-to-line [Fe/H] dispersion and the $\Delta \xi_{\text{mic}}$ value was estimated from the $\log \epsilon(\text{FeI})$ versus line strength plots.

Abundance differences were calculated between the values listed in Table 2 and those derived from changes in the model atmosphere parameters. These values were added in quadrature, along with the error of the mean for each species in order to roughly account for $\log(gf)$ uncertainties, and are reported in Table 3. Note that for cases where only one line was available, we adopted a common fitting error of 0.05 dex. For elements listed in Table 3 that are normalized relative to FeI, or FeII for species in the dominant ionization state, the correlated changes in $\log \epsilon(X)$ and $\log \epsilon(\text{FeI})$ or $\log \epsilon(\text{FeII})$ are taken into account.

Additional sources of uncertainty, such as departures from LTE, 1D versus 3D model atmosphere effects, spheri-

³ The grid is available at: <http://wwwuser.oats.inaf.it/castelli/grids.htm>

⁴ The MOOG source code is available at: <https://www.as.utexas.edu/~chris/moog.html>.

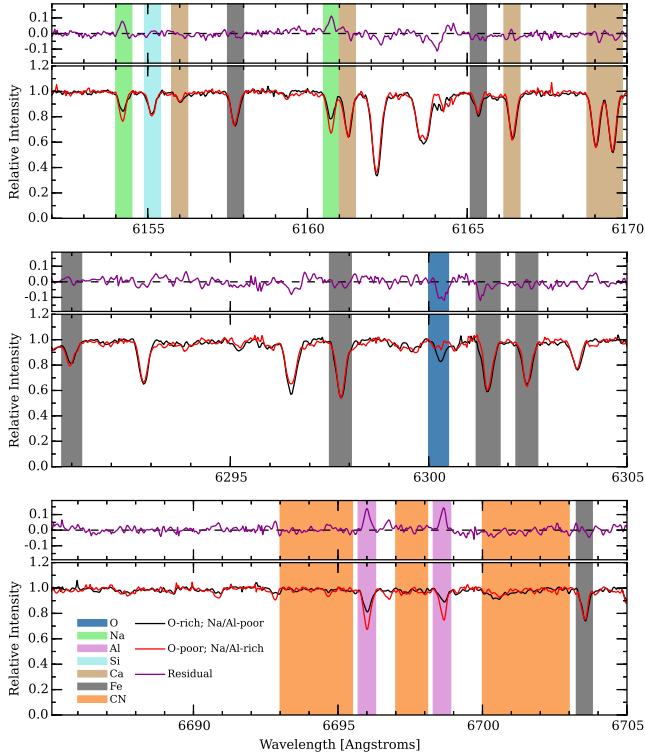


Figure 3. Two sample M2FS spectra are shown illustrating the typical data quality and line strength variations of several light elements. The black (2M17374273–0315238) and red (2M17373815–0314496) spectra represent stars with similar T_{eff} , $\log(g)$, and $[\text{Fe}/\text{H}]$ but very different light element compositions. The shaded regions indicate lines of O, Na, Al, Si, Ca, Fe, and molecular CN. Note that the variable line strengths of the V/Ti blend near 6296.5 Å are due to the merging of two spectrograph orders. Residual plots are shown in dark magenta above each set of sample spectra.

cal versus plane parallel calculations, and modifications to the model atmosphere structure as a result of changes in detailed composition, were not taken into account. Many of these effects likely cancel out due to the relative nature of the present analysis, which was carried out differentially with respect to the metal-poor giant Arcturus, and the small temperature, gravity, and metallicity range of the target stars. One systematic issue that could affect a portion of our sample is the influence of He enhancement on stellar structure and line formation. As will be described in Section 5, about 1/4 of our sample may be significantly He-enriched. Boehm-Vitense (1979) showed that in cool giants an increase in He abundance is most likely to affect (strengthen) the neutral atomic lines of elements with low first ionization potentials, such as Na or Ca. However, several authors (e.g., Piotto et al. 2005; Johnson et al. 2009; Cunha et al. 2010) have demonstrated that He abundances as high as $Y \sim 0.4$ likely have little effect on the derived $[\text{X}/\text{Fe}]$ ratios for most elements.

5 RESULTS AND DISCUSSION

5.1 Composition Overview

Previous $[\text{Fe}/\text{H}]$ estimates for NGC 6402 are based on photometric analyses of cluster CMDs (e.g., Contreras Peña et al. 2013; Nataf et al. 2013; Contreras Peña et al. 2018) and find $[\text{Fe}/\text{H}] \sim -1.1$ to -1.4 dex. The spectroscopic results presented in Table 2 are in agreement with past work as we find a mean $[\text{Fe}/\text{H}] = -1.13$ dex ($\sigma = 0.05$ dex), based on a sample of 35 stars. The small $[\text{Fe}/\text{H}]$ dispersion of 0.05 dex indicates that, despite being among the most massive and luminous clusters in the Galaxy, NGC 6402 does not possess a significant intrinsic metallicity spread.

The overall composition characteristics of NGC 6402 are summarized with the box plot shown in Fig. 4. The figure clearly demonstrates that the light element ratios $[\text{O}/\text{Fe}]$, $[\text{Na}/\text{Fe}]$, and $[\text{Al}/\text{Fe}]$ exhibit significant star-to-star variations. In fact, the full abundance ranges of $[\text{O}/\text{Fe}]$, $[\text{Na}/\text{Fe}]$, and $[\text{Al}/\text{Fe}]$ are 1.61, 0.89, and 1.24 dex, respectively. The clear line strength changes displayed in Fig. 3 indicate that the light element abundance variations are real and not an artifact of the analysis methods. Smaller but real variations seem to be present for at least $[\text{Mg}/\text{Fe}]$ and $[\text{Si}/\text{Fe}]$ as well. Despite these moderate variations, the cluster is generally α -enhanced with $\langle[\text{Mg}/\text{Fe}]\rangle = +0.34$ dex ($\sigma = 0.10$ dex), $\langle[\text{Si}/\text{Fe}]\rangle = +0.34$ dex ($\sigma = 0.10$ dex), and $\langle[\text{Ca}/\text{Fe}]\rangle = +0.31$ dex ($\sigma = 0.07$ dex).

Unlike the lighter elements, the Fe-peak elements Cr and Ni exhibit approximately solar ratios with $\langle[\text{Cr}/\text{Fe}]\rangle = +0.07$ dex ($\sigma = 0.07$ dex) and $\langle[\text{Ni}/\text{Fe}]\rangle = -0.11$ dex ($\sigma = 0.06$ dex). The heavier neutron-capture elements La and Eu both exhibit enhanced ratios with $\langle[\text{La}/\text{Fe}]\rangle = +0.29$ dex ($\sigma = 0.08$ dex) and $\langle[\text{Eu}/\text{Fe}]\rangle = +0.37$ dex ($\sigma = 0.09$ dex). The moderately low mean $[\text{La}/\text{Eu}] = -0.08$ dex and 0.1 dex dispersion suggest that the heavy element pollution within NGC 6402 was well-mixed and did not contain significant enrichment from the slow neutron-capture process.

A comparison of the mean abundance distributions shown in Fig. 4 with the typical composition characteristics found in other inner Galaxy globular clusters (e.g., see Fig. 9-10 of Johnson et al. 2018) indicates that NGC 6402 follows the common trend of $[\alpha/\text{Fe}] \sim +0.3$ dex, $[\text{Fe-peak}/\text{Fe}] \sim +0.0$ dex, and $[\text{La}/\text{Eu}] < 0.0$ dex. The heavier α , Fe-peak, and neutron-capture element data are also consistent with bulge and disk field stars of similar $[\text{Fe}/\text{H}]$ found within the inner Galaxy (e.g., Johnson et al. 2014; Bensby et al. 2017). This suggests that the primordial gas from which NGC 6402 formed possessed a composition similar to the Milky Way field populations near $[\text{Fe}/\text{H}] \sim -1$. However, a more detailed examination of NGC 6402’s light element composition reveals a particularly interesting formation history.

5.2 Identifying Multiple Populations via Light Element Variations

As mentioned in Section 1, globular clusters are generally composed of two or more populations with different light element compositions. However, detailed comparisons of subpopulations within different systems are difficult to interpret because no specific set of chemical properties define the various cluster components. Furthermore, nomenclature varies

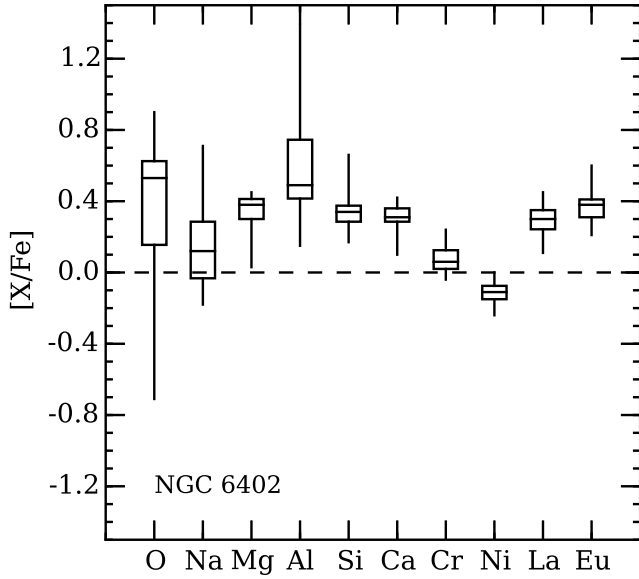


Figure 4. A box plot is shown illustrating the $[X/Fe]$ distributions of all elements analyzed here. The top, middle, and bottom horizontal lines for each box illustrate the first, second (median), and third quartiles of the $[X/Fe]$ distribution. The vertical lines indicate the minimum and maximum $[X/Fe]$ ratios.

among authors with little agreement existing beyond the notion that “first” generation/population stars have compositions similar to halo field stars and “second” generation/population stars exhibit higher He, N, and Na with lower C and O abundances. For the purposes of this work we have adopted the nomenclature of Carretta (2015), which identified at least five independent groups in NGC 2808 associated with primordial (“halo-like”: P1/P2), intermediate (diluted: I1/I2), and extreme (pure polluted material: E) compositions. We also adopt the interpretation presented by D’Antona & Ventura (2007), Milone et al. (2015b), and D’Antona et al. (2016) that the P1 group is the sole primordial population, the P2, I1, and I2 stars represent diluted second generation compositions, and that the E second generation stars trace a combination of heavy pollution and possibly some *in situ* mixing. Note that the P1, P2/I1, I2, and E groups may be equivalent to the B, C, D, and E populations identified in Milone et al. (2015b), respectively.

As illustrated in Fig. 5, the NGC 6402 data were partitioned into sub-populations using each star’s $[O/Na]$ ratio⁵. The bottom panel of Fig. 5 further indicates that the P1+P2 and E groups are easily distinguished using any combination of O, Na, and Al abundances, but the P1/P2 separation is more ambiguous. The $[O/Na]$ dispersion for stars with $[O/Na] > 0.0$ dex is 0.24 dex, which is ~ 30 per cent larger than the mean $[O/Na]$ measurement error estimated from the individual $[O/Fe]$ and $[Na/Fe]$ values provided in Table 3. The broad and potentially bimodal $[O/Na]$ distribution shown in the top panel of Fig. 5 suggests either that two low-Na populations are present or that the P1+P2 group is not homogeneous in composition.

⁵ For cases in which $[O/Fe]$ or $[Na/Fe]$ could not be measured, identification as a P1, P2, or E star was based on $[Al/Fe]$.

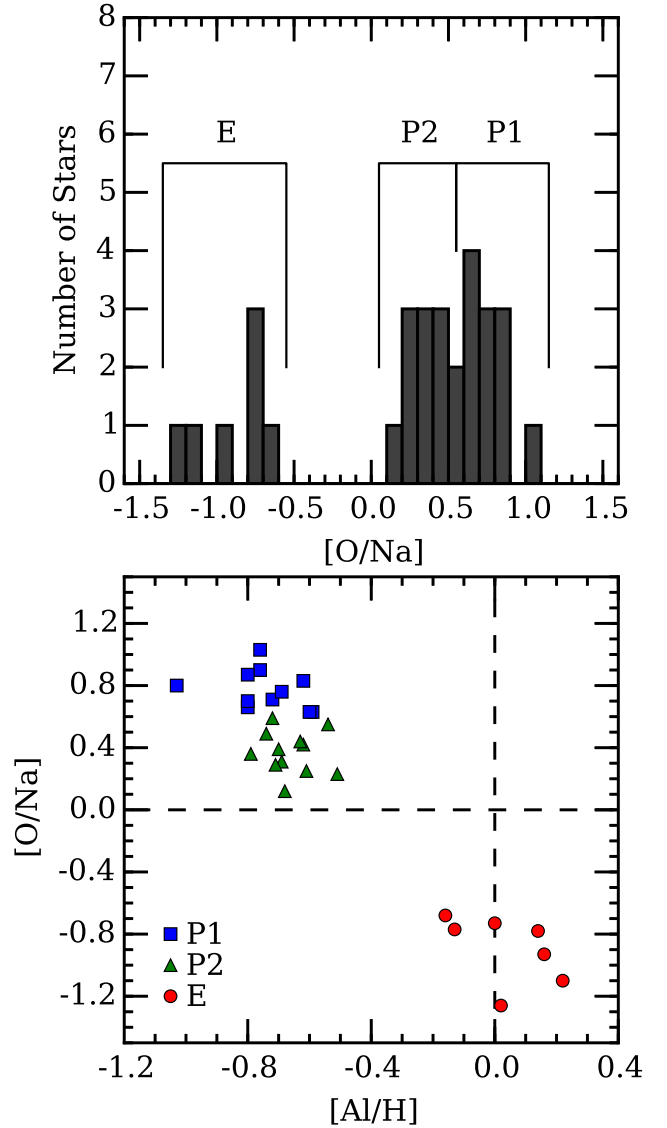


Figure 5. *Top:* a histogram of $[O/Na]$ ratios for NGC 6402 indicates the chemical distinction between P1, P2, and E population stars. The data are sampled using 0.1 dex bins. Note the paucity of stars with $-0.6 < [O/Na] < +0.1$ that match the typical I1 and I2 groups. *Bottom:* $[O/Na]$ is plotted as a function of $[Al/H]$ to illustrate the composition differences between P1, P2, and E stars.

Photometric evidence from *HST* “chromosome” maps suggests that intrinsic composition variations may be present among first generation stars in some clusters. However, no clear correlation exists between the observed color dispersions and variations in $[O/Fe]$ or $[Na/Fe]$ for first generation stars, which suggests that the color extensions may only reflect changes in He and/or N (Milone et al. 2017, 2018; Lardo et al. 2018). Since the P1 and P2 groups identified here exhibit nearly identical O-Na distributions as those presented in Carretta (2015) for NGC 2808 (see also Section 5.4) and Milone et al. (2015b) find the NGC 2808 P1 and P2 stars to exhibit very different near-UV/optical colors, we conclude that the NGC 6402 stars with $[O/Na] > 0.0$ dex form two distinct populations. Further evidence supporting

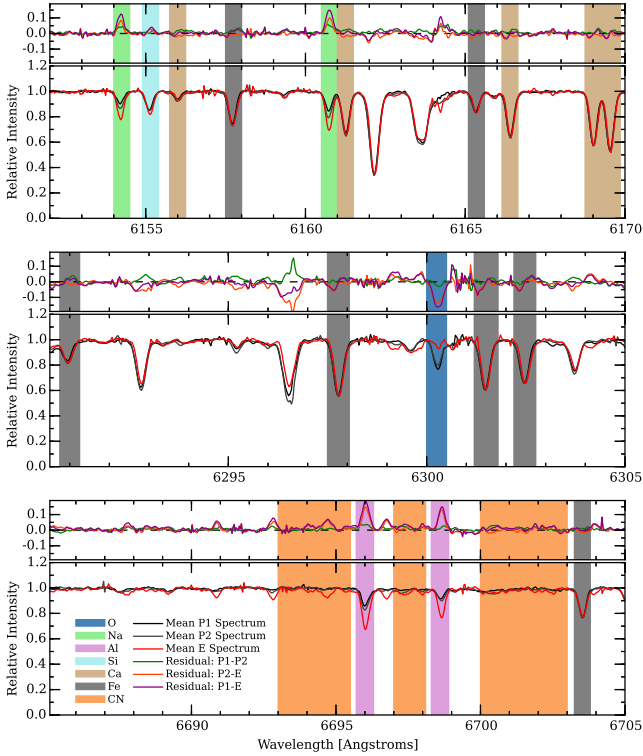


Figure 6. Similar to Fig. 3, mean combined spectra for stars in the P1, P2, and E groups with $T_{\text{eff}} \sim 4300$ K (~ 6 stars in each group) are compared. Line depth residuals for the P1–P2, P2–E, and P1–E mean spectrum pairs are illustrated with the green, dark orange, and dark magenta lines, respectively. Note the significant variations in O, Na, Al, and CN line depths between especially the P1 and E groups.

clear composition differences between the P1 and P2 stars can be seen in the combined spectra of Fig. 6 where the P2 population exhibits weaker O and stronger Na/Al lines.

Table 4 outlines the mean chemical properties of the P1, P2, and E groups and shows that many of the composition differences are of high statistical significance. As was already evident from Fig. 5, results from a Welch’s t-test analysis indicate that significant differences exist between the various NGC 6402 populations when considering [O/Fe], [Na/Fe], and [Al/Fe]. However, the P1 and P2 groups exhibit similar [Mg/Fe] and [Si/Fe] abundances while the E population has significantly lower [Mg/Fe] and higher [Si/Fe]. Similarly, the E group has higher [Ca/Fe] than the P1 population, but the data are inconclusive regarding whether the P2 [Ca/Fe] abundances differ from the P1 and/or E populations. For elements heavier than Ca, Table 4 indicates that the various sub-populations are chemically indistinguishable (see also Fig. 6).

5.2.1 Population Ratios

Recent large sample analyses by Carretta et al. (2009a) and Milone et al. (2017) revealed several global trends: (1) globular clusters are numerically dominated by intermediate composition stars; (2) most clusters have first generation fractions of ~ 30 – 40 per cent; (3) the fraction of first generation stars strongly declines as a function of increasing

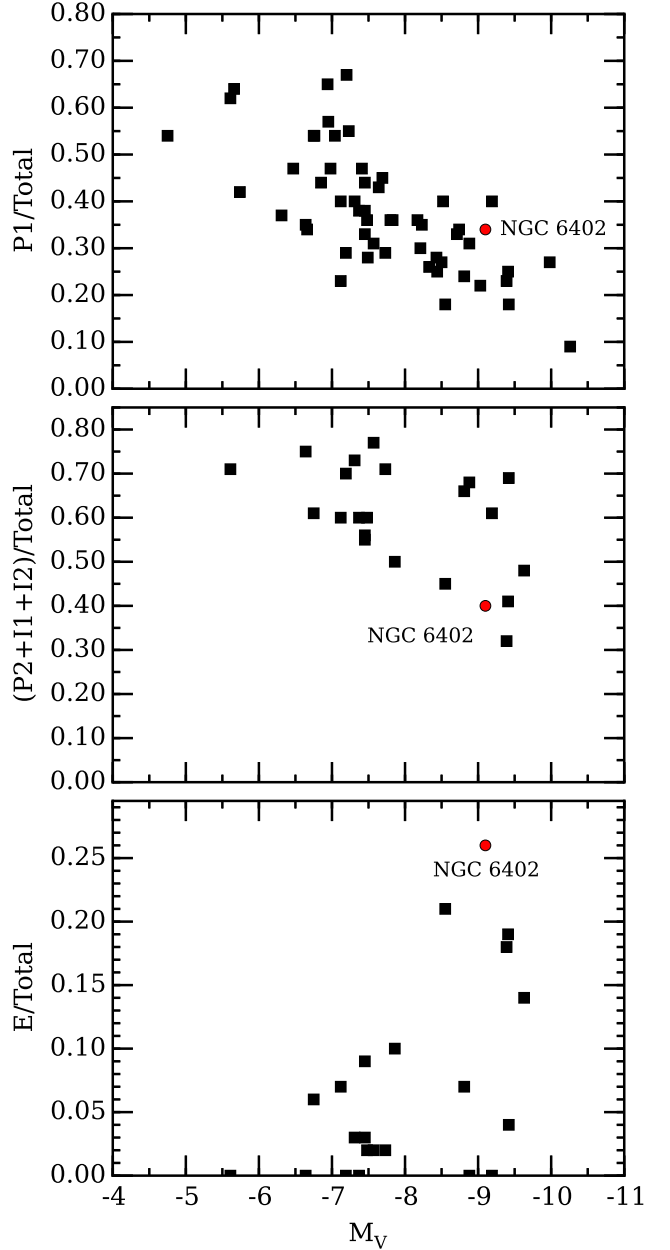


Figure 7. The observed ratios of first generation (P1; top panel), intermediate second generation (P2, I1, and I2; middle panel), and extreme second generation (E; bottom panel) stars relative to the cluster totals are plotted as a function of each cluster’s absolute magnitude (a tracer for mass). Data are shown for various literature sources (filled black boxes) and NGC 6402 (filled red circles). The literature data for first generation stars are from Milone et al. (2017) while the intermediate and extreme second generation ratio data are from Carretta et al. (2009a).

present-day mass; and (4) extreme second generation stars with very low [O/Fe] are rare, predominantly located in the most massive clusters with extended blue HBs, and when found are present at only the 5–20 per cent level. Fig. 7 summarizes these observations and shows that the intermediate composition ratio generally declines with increasing cluster mass as well.

For NGC 6402, we find the P1, P2, and E groups to

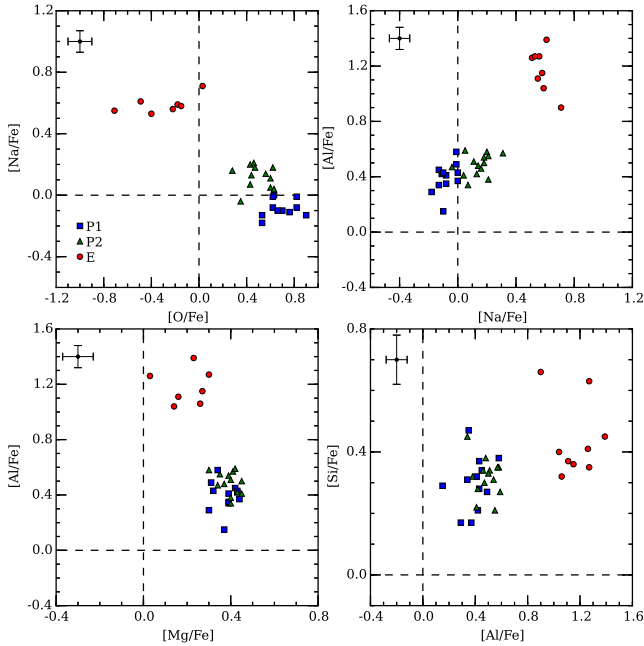


Figure 8. Combinations of $[O/Fe]$, $[Na/Fe]$, $[Mg/Fe]$, $[Al/Fe]$, and $[Si/Fe]$ are plotted for NGC 6402. In all panels the filled blue boxes, green triangles, and red circles indicate stars belonging to the P1, P2, and E populations, respectively, following the notation from Carretta (2015). Note the large abundance gap present for all element combinations.

represent 34 per cent (12/35), 40 per cent (14/35), and 26 per cent (9/35) of our sample, respectively. Fig. 7 indicates that these population ratios are in general agreement with the bulk trend observed for other Galactic globular clusters. Interestingly, the extreme population fraction in NGC 6402 may be among the highest of any known cluster. Although the presence of extreme composition stars is not surprising given the cluster’s extended blue HB, we note that similar mass clusters generally contain large populations of I1 and I2 stars as well. However, Fig. 5 indicates that the I1/I2 intermediate composition stars may be entirely absent from NGC 6402. As a result the P2 fraction may be unusually high in NGC 6402, especially when compared against the NGC 2808 P2 component that constitutes only 25 per cent of the Carretta (2015) sample.

5.3 Light Element (Anti-)correlations

Fig. 8 shows that NGC 6402 exhibits the same light element (anti-)correlations that are present in nearly all massive globular clusters. Similar to other clusters with extended blue HBs, the (anti-)correlated abundance patterns in NGC 6402 are present not only for $[O/Fe]$ and $[Na/Fe]$ but extend to $[Mg/Fe]$, $[Al/Fe]$, and $[Si/Fe]$ as well. However, (anti-)correlations involving $[Mg/Fe]$ and $[Si/Fe]$ are driven solely by the E population. As established in Section 5.2 and reinforced through Fig. 8, the P1 and P2 populations exhibit noticeably different $[O/Fe]$, $[Na/Fe]$, and $[Al/Fe]$ abundances but indistinguishable $[Mg/Fe]$ and $[Si/Fe]$.

An examination of Fig. 2 in Prantzos et al. (2007) indicates that, depending on the He abundance of the P2 group, temperatures as low as 45–60 MK could be sufficient to mod-

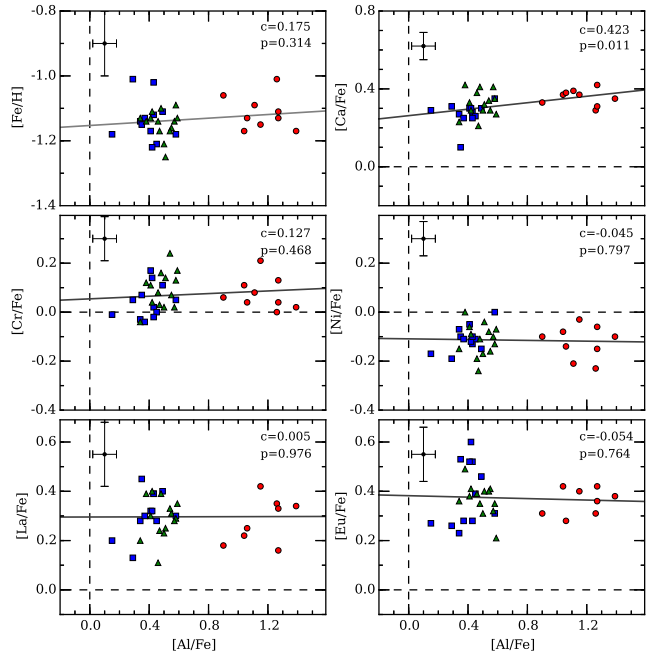


Figure 9. Similar to Fig. 8, $[Fe/H]$, $[Ca/Fe]$, $[Cr/Fe]$, $[Ni/Fe]$, $[La/Fe]$, and $[Eu/Fe]$ are plotted as a function of $[Al/Fe]$. The solid grey lines show the best-fit linear functions through each distribution. The numerical “c” and “p” values provided in each panel are the Pearson correlation coefficients and associated statistical p-values from the fits. Note that only $[Ca/Fe]$ shows any evidence supporting a statistically significant correlation with $[Al/Fe]$.

ify P1 composition gas such that $[O/Fe]$ declines, $[Na/Fe]$ and $[Al/Fe]$ increase, and $[Mg/Fe]$ and $[Si/Fe]$ remain unchanged. If burned at 45–60 MK, the ^{25}Mg and ^{26}Mg isotopes could be particularly powerful temperature discriminators. However, previous work on other clusters has shown that clear variations in the ^{24}Mg , ^{25}Mg , and ^{26}Mg isotope ratios are only detected when $[Al/Fe]$ enhancements are large (e.g., Shetrone 1996; Yong et al. 2003; Sneden et al. 2004; Da Costa et al. 2013; Ventura et al. 2018). Although the P2 gas could have been burned at higher temperatures and then diluted with “pristine” P1 composition material, no single dilution model fits through the P1, P2, and E populations shown in Fig. 8 (see also Section 5.4). Therefore, we conclude that the P2 group is not a result of simple dilution between P1 and E composition gas and instead represents an independent pollution event.

As mentioned above, the Mg-Al anti-correlation and Al-Si correlation shown in Fig. 8 are driven by composition differences between the P1+P2 and E populations. Nucleosynthesis studies have shown that significant changes to the $[Mg/Fe]$ and $[Si/Fe]$ abundances can only occur when burning temperatures exceed ~ 65 MK (e.g., Karakas & Lattanzio 2003; Prantzos et al. 2007, 2017; Ventura et al. 2018). These results therefore place a lower limit of about 65 MK on the burning conditions responsible for producing the gas from which the E population formed, and indicate further that the P1, P2, and E groups in NGC 6402 did not originate from a single pollution source (see also Section 5.4).

Interestingly, Fig. 9 shows that the correlated abundance variations may reach to elements as heavy as Ca since a potentially significant correlation between $[Al/Fe]$

and $[\text{Ca}/\text{Fe}]$ is detected. Furthermore, the Welch's t-test results summarized in Table 4 indicate with high confidence that the mean $[\text{Ca}/\text{Fe}]$ abundance is higher in the E population than the P1 group. A marginal detection of the P2 population having a higher mean $[\text{Ca}/\text{Fe}]$ abundance than the P1 group is also observed; however, we consider this result to be spurious since neither $[\text{Mg}/\text{Fe}]$ nor $[\text{Si}/\text{Fe}]$ vary significantly between the P1 and P2 stars. If the Al-Ca correlation is confirmed, NGC 6402 would join clusters such as NGC 2808 (Carretta 2015; Mucciarelli et al. 2015) and NGC 2419 (Cohen & Kirby 2012; Mucciarelli et al. 2012) in possessing light element correlations that extend to elements heavier than Si. Such a confirmation would indicate that the gas from which the E population stars in NGC 6402 formed was processed at temperatures >100 MK (Ventura et al. 2012; Iliadis et al. 2016).

However, we stress two important caveats related to the Al-Ca correlation detection: (1) Table 4 shows that the mean difference in $[\text{Ca}/\text{Fe}]$ between the P1 and E groups is only 0.09 dex and therefore noticeably smaller than the P1-E $[\text{X}/\text{Fe}]$ differences involving lighter elements; and (2) the Al/Ca-rich population is likely He-enhanced, and as mentioned in Section 4.3 neutral Ca is one of the species that may be susceptible to line strength enhancements due to changes in the He mass fraction. Stronger confirmation of very high temperature burning in NGC 6402 may be obtained by searching for similar correlations involving Sc and/or K. These elements have been shown to vary in at least NGC 2808 and NGC 2419 (Cohen & Kirby 2012; Mucciarelli et al. 2012; Carretta 2015; Mucciarelli et al. 2017) and possess stronger correlation signatures owing to their intrinsically lower abundances.

5.3.1 Missing Intermediate Composition Stars

The most notable observation from Fig. 8 is the paucity of intermediate composition (I1/I2) stars having $[\text{O}/\text{Fe}] \sim +0.1$ dex, $[\text{Na}/\text{Fe}] \sim +0.3$ dex, and $[\text{Al}/\text{Fe}] \sim +0.8$ dex. The discrete nature of the light element (anti-)correlations shown in Fig. 8 is not surprising, but previous analyses have shown that clusters do not generally have E composition stars without significant populations of I1/I2 composition stars (e.g., Carretta et al. 2009a). In fact, the ω Cen groups with $[\text{Fe}/\text{H}] \gtrsim -1.3$ are the only other populations that exhibit a large number of E composition stars with a simultaneous paucity of I1/I2 stars (Johnson & Pilachowski 2010; Marino et al. 2011c)⁶. However, we note that a similar composition gap could also be present in NGC 2419 based on analyses of the cluster's HB morphology (di Criscienzo et al. 2011) and the UVES sample of Mucciarelli et al. (2015).

The unusual light element composition of NGC 6402 is further emphasized in Fig. 10 where we compare the cluster's $[\text{O}/\text{Fe}]$ and $[\text{Na}/\text{Fe}]$ abundances against those of other similar metallicity clusters shifted onto the same scale⁷. When

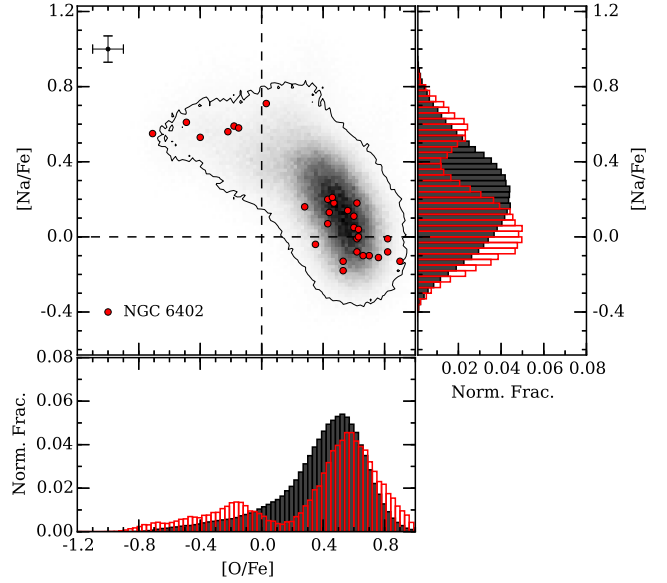


Figure 10. The $[\text{Na}/\text{Fe}]$ abundances for NGC 6402 (filled red circles) are plotted as a function of $[\text{O}/\text{Fe}]$ and compared against similar clusters (density plot) with $-1.3 < [\text{Fe}/\text{H}] < -0.8$ from Carretta et al. (2009a,b), Yong et al. (2014a), Carretta (2015), Lapenna et al. (2015), and Johnson et al. (2017a, 2018). The literature sources were shifted to have approximately the same upper $[\text{O}/\text{Fe}]$ and lower $[\text{Na}/\text{Fe}]$ bounds as NGC 6402, and were resampled 10^4 times. Each resampling was convolved with a Gaussian error distribution of 0.1 dex in $[\text{X}/\text{Fe}]$. The contour outlines a region where 95 per cent of the resampled literature data reside. Histograms for the literature (grey) and similarly resampled NGC 6402 data (red) are shown for both $[\text{O}/\text{Fe}]$ and $[\text{Na}/\text{Fe}]$.

convolved with a typical measurement uncertainty of 0.1 dex and resampled to produce a probability distribution, we find that NGC 6402 exhibits both a very extended O-Na anticorrelation and a paucity of the most common intermediate composition stars found in clusters with $[\text{Fe}/\text{H}] \sim -1$. Fig. 10 also indicates that even if other clusters actually have bimodal O-Na distributions, the mean differences between the two groups are not as extreme as in NGC 6402.

An important question to address is whether the composition gaps shown in Fig. 8 and Fig. 10 are real or due to sampling effects. Since the O-Na distribution from Fig. 8 includes 32 stars for NGC 6402, we investigated the influence of sampling by performing 10^5 random drawings of 32 stars, each with an added random Gaussian error distribution ($\sigma = 0.1$ dex), from two different parent populations. The first population from which samples were drawn followed the literature distribution shown in Fig. 10, which is relatively smooth and peaks near the observed gap in NGC 6402. The second population from which samples were drawn traced the clumpy and extended NGC 2808 distribution from Carretta (2015). In each case, we measured the frequency with which the random drawings selected at least 7 E composition stars and also failed to include any stars within

⁶ Similar composition gaps have been found in a few other clusters (e.g., Carretta et al. 2014), but these cases tend to have sample sizes of ~ 10 stars or fewer. Clusters such as M 4 (Marino et al. 2008; Villanova & Geisler 2011) also exhibit significant composition gaps but do not contain E stars.

⁷ The literature $[\text{O}/\text{Fe}]$ and $[\text{Na}/\text{Fe}]$ data have been shifted by

eye to have approximately the same mean composition as the “P1” group (see Section 5.2.1) in NGC 6402. These shifts aim to minimize systematic effects due to the use of different solar abundances, line lists, analysis methods, and non-LTE corrections.

the ([O/Fe],[Na/Fe]) coordinates (+0.2,+0.8), (-0.35,+0.4), (+0.1,+0.1), and (+0.6,+0.5).

For the first distribution, only 0.004 per cent of the simulations produced an O-Na gap similar to that observed in NGC 6402. Similarly, the second distribution produced a gap with a frequency of only 0.057 per cent. We also found that for a sample size of 32 the expected numbers of stars residing in the O-Na gap of Fig. 10 are 9 and 6 if the parent populations trace the continuous and clumpy (NGC 2808) distributions, respectively. A combination of measurement uncertainty and/or stochastic enrichment will likely produce at least some I1/I2 stars in a larger sample of NGC 6402. However, the present data indicate a low probability that NGC 6402's true O-Na distribution contains a significant number of I1/I2 stars. Fig. 1 does not reveal any clear observational bias, and the mean spectra illustrated in Fig. 6 show a substantial change in O and Na line strengths between the P2 and E groups. If I1/I2 stars are present in NGC 6402 then we estimate an upper limit of only ~10–15 per cent of the total cluster population, which is far lower than the ~25 per cent occurrence rate in NGC 2808 (Carretta 2015).

5.4 Nucleosynthesis Implications from a Comparison with NGC 2808

In Fig. 11 we compare the relative abundance changes ($\Delta[X/Fe]$) in [O/Fe], [Na/Fe], [Mg/Fe], [Al/Fe], [Si/Fe], and [Ca/Fe] between the P1 and other sub-populations for NGC 6402 and NGC 2808. The two clusters share similar present-day masses, ages, mean [Fe/H] values, extended blue HBs, and exhibit spectroscopic evidence of various populations with unique chemical compositions (e.g., Carretta 2015; Carretta et al. 2018). However, their detailed composition patterns are not the same.

The $\Delta[O/Fe]-\Delta[Na/Fe]$ panel in Fig. 11 best illustrates the missing I1/I2 population of NGC 6402 compared to NGC 2808, and shows that despite the composition gap the relative O-Na distributions for the P1, P2, and E groups between the two clusters are nearly identical. However, the NGC 6402 $\Delta[Mg/Fe]$, $\Delta[Al/Fe]$, and $\Delta[Si/Fe]$ values for the E group are lower than in NGC 2808 by approximately 0.25 dex, 0.7 dex, and 0.05 dex, respectively. To first order, the E population composition differences between NGC 6402 and NGC 2808 can be understood in terms of burning temperatures.

For example, Fig. 12 utilizes the nucleosynthesis calculations of Prantzos et al. (2007) to show that the E group $\Delta[O/Fe]$ and $\Delta[Na/Fe]$ values for both clusters may be well described using burning temperatures of at least 70–80 MK. However, the significantly larger $\Delta[Mg/Fe]$ and $\Delta[Al/Fe]$ values reached by NGC 2808's E population suggest the cluster was predominantly polluted by gas reaching at least 75–80 MK. In contrast, the NGC 6402 E population data are better fit with a burning temperature of ~70 MK. A higher burning temperature for the E population in NGC 2808 is also consistent with its larger Si enhancements since ^{28}Si production is a relatively monotonic function of temperature in the ~65–125 MK range (e.g., Prantzos et al. 2017). As a consequence of the very high temperatures required to modify elements heavier than Si, the Al-Ca correlation signature observed in NGC 6402, but not NGC 2808, seems likely to be a spurious result.

Interestingly, Fig. 12 shows that Mg destruction and

Na/Al production are strong functions of the hydrogen exhaustion (H_{ex}) value, which is used as a proxy for burning time or extent. Although NGC 6402 and NGC 2808 are largely fit by the 70–80 MK dilution curves when $H_{\text{ex}} = 0.01$, such low values may not permit sufficient He production to explain the 0.10–0.15 He mass fraction (ΔY) enhancements likely present in the E populations of each cluster. Larger H_{ex} values can also fit the data, but at least for NGC 6402 such a scenario would require additional dilution to decrease the maximum $\Delta[Na/Fe]$ and $\Delta[Al/Fe]$ ratios. We note that Prantzos et al. (2017) did include a small initial dilution of 4–5 per cent pristine material to explain the light element variations in NGC 2808. Small H_{ex} values may be acceptable if additional gas with the proper composition (e.g., He-enhanced) was present in the early cluster environment from sources such as Wolf-Rayet stars (e.g., Smith 2006) or Luminous Blue Variables (e.g., Dufour et al. 1997; Smith & Morse 2004). Such a scenario could boost the E population's He abundance to higher levels than would be expected based on the abundances of other light elements alone. Temperatures exceeding 80 MK also lower the Na and Al yields but may destroy too much Mg and produce too much Si to fit the observations (e.g., see Fig. 3 of Prantzos et al. 2017).

Further inspection of Fig. 11 and Fig. 12 indicates that [Al/Fe] abundance differences between NGC 6402 and NGC 2808 extend to the P2 populations as well. None of the nucleosynthesis dilution curves in Fig. 12 pass through both the P2 and E groups of either cluster, and the $\Delta[Na/Fe]-\Delta[Al/Fe]$ plots in particular seem to rule out that the P2 and E stars could have originated from the same pollution sources. These observations reinforce the conclusion by Carretta et al. (2018) that at least NGC 2808 cannot be fit by a simple dilution model, and we conclude that at least two different enrichment sources are required to explain the NGC 2808 and NGC 6402 data. Although the pure hydrostatic burning curves provide an unsatisfactory explanation for the P2 composition stars in both clusters, the Ventura et al. (2013) AGB models shown in the bottom rows of Fig. 12 are a better fit.

AGB models struggle to reproduce the abundance patterns of the E populations in most clusters⁸, but are capable of explaining a majority of the intermediate composition stars. Fig. 12 shows that the NGC 2808 P2, I1, and I2 stars are well-fit by the products of 5.5–7 M_{\odot} AGB ejecta, but the NGC 6402 P2 stars are not completely fit by any single model set. However, the NGC 6402 P2 stars would be consistent with the dilution curves from the 7–8 M_{\odot} AGB models if the O and/or Na yields from the 7.5 M_{\odot} AGB model or the Al yield from the 7 M_{\odot} AGB model could be reduced. The new calculations presented in Di Criscienzo et al. (2018) provide a decrease in [Na/Fe] for the 7–7.5 M_{\odot} models, but the substantial increase in [Al/Fe] precludes these calculations from improving the fits in Fig. 12. Regardless of the modeling difficulty, we conclude that the P2 composition stars in NGC 6402 were polluted

⁸ Strong Mg depletion is a particular problem, especially at higher metallicities (e.g., D'Antona et al. 2016), but may be remedied with updated models (Di Criscienzo et al. 2018).

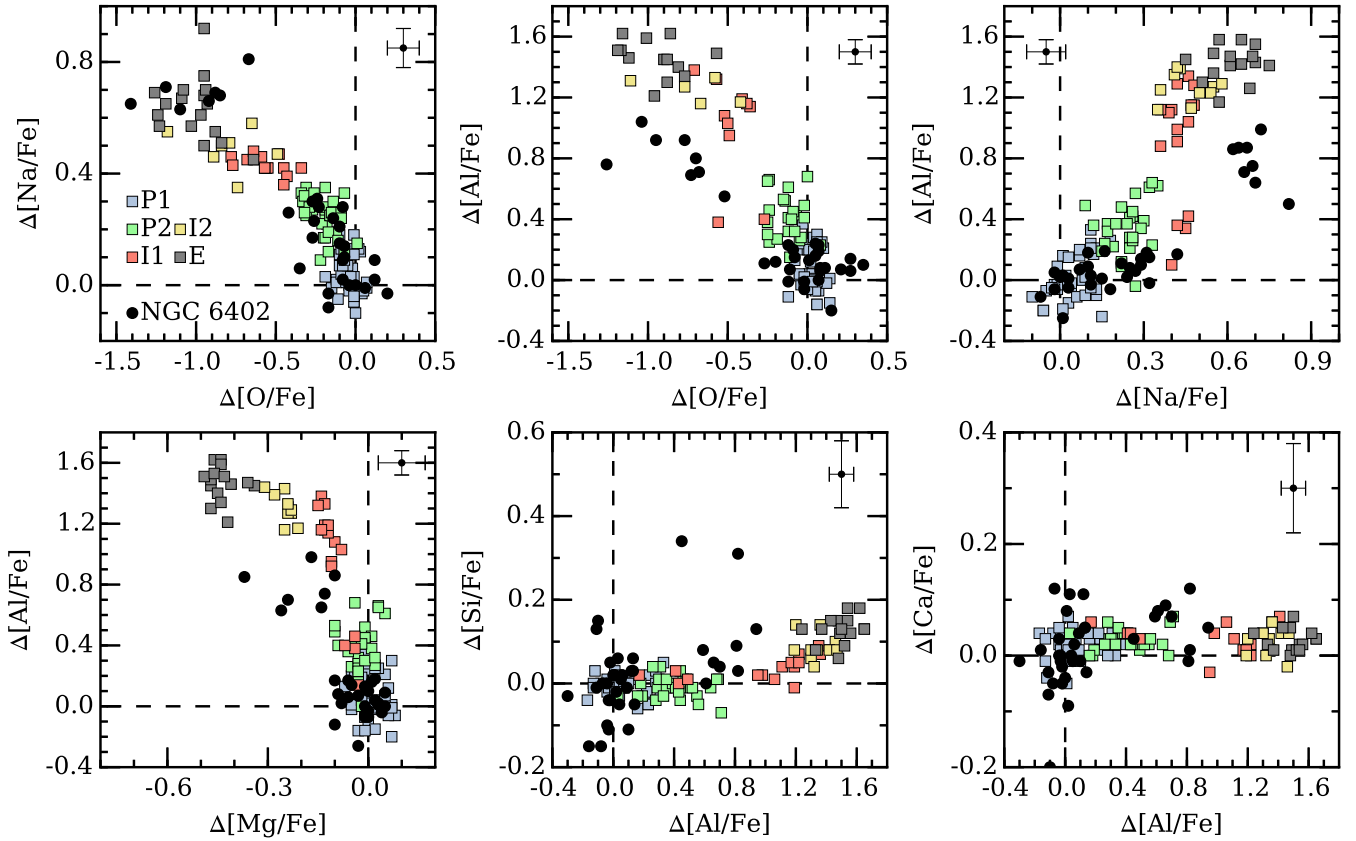


Figure 11. NGC 6402 (filled black circles) and NGC 2808 (filled boxes) chemical abundance data are compared using combinations of $\Delta[\text{O}/\text{Fe}]$, $\Delta[\text{Na}/\text{Fe}]$, $\Delta[\text{Mg}/\text{Fe}]$, $\Delta[\text{Al}/\text{Fe}]$, $\Delta[\text{Si}/\text{Fe}]$, and $\Delta[\text{Ca}/\text{Fe}]$ where $\Delta[\text{X}/\text{Fe}]$ represents the difference between a star's $[\text{X}/\text{Fe}]$ ratio and the cluster's assumed primordial composition. The NGC 2808 data and population classifications (P1, P2, I1, I2, and E) are from Carretta (2015) and Carretta et al. (2018). The NGC 6402 and NGC 2808 data have been shifted to have the same mean $[\text{X}/\text{Fe}]$ ratios for the P1 groups. See text for details.

by a different class or (higher?) mass range of objects than those in NGC 2808.

5.5 Impact of Light Element Variations on Post-RGB Evolution

Several authors have demonstrated a close connection between the magnitude of a globular cluster's light element variations and the color/temperature extent of its HB (e.g., Carretta et al. 2007; Gratton et al. 2010; Milone et al. 2014). Although the detailed morphology of a cluster's HB is a complicated mixture of age, metallicity, He abundance, rotation, RGB mass loss, and several atmospheric effects (e.g., Catelan 2009), some additional insight may be gained by examining cluster sets that minimize differences between these parameters. A cluster such as NGC 6402, which appears to be missing a normally well-populated stellar group, may also provide insight into the connection between light element composition and HB location.

An RGB star's detailed composition is closely tied to its eventual location on the HB (e.g., Marino et al. 2011b; Gratton et al. 2011, 2013, 2014; Marino et al. 2014; Gratton et al. 2015). The coolest HB stars frequently exhibit abundance patterns similar to those of the P1 RGB group while warmer HB stars tend to have lower O and Mg abundances along with higher N, Na, and Al abundances.

However, the exact distribution is not the same for all clusters. For example, red HB stars show clear signatures of light element abundance variations in some clusters (e.g., Gratton et al. 2013; Marino et al. 2014) but exhibit homogeneous compositions in others (e.g., Marino et al. 2011b; Gratton et al. 2013). In some cases, red HB, RR Lyrae, and/or the coolest blue HB stars may all contain P1 composition stars (e.g., Marino et al. 2011b; Gratton et al. 2015). Interestingly, the only stable observation is that for clusters with extended blue HBs the most polluted HB stars are found at the highest temperatures. The generally accepted explanation is that He enhancement, in addition to cluster age and metallicity, drive the high temperature tail of a cluster's blue HB morphology (e.g., D'Antona et al. 2002; Gratton et al. 2010; Milone et al. 2014).

With these observations in mind, Fig. 13 compares the RGB and HB morphologies of NGC 2808 and NGC 6402, which as noted previously have similar ages, masses, metallicities⁹, and to some extent light element compositions. However, we note that despite these similarities the detailed HB morphologies are different.

⁹ In addition to direct spectroscopic measurements, the similar red HB and RGB bump luminosities shown in Fig. 13 further support both clusters exhibiting comparable mean metallicities.

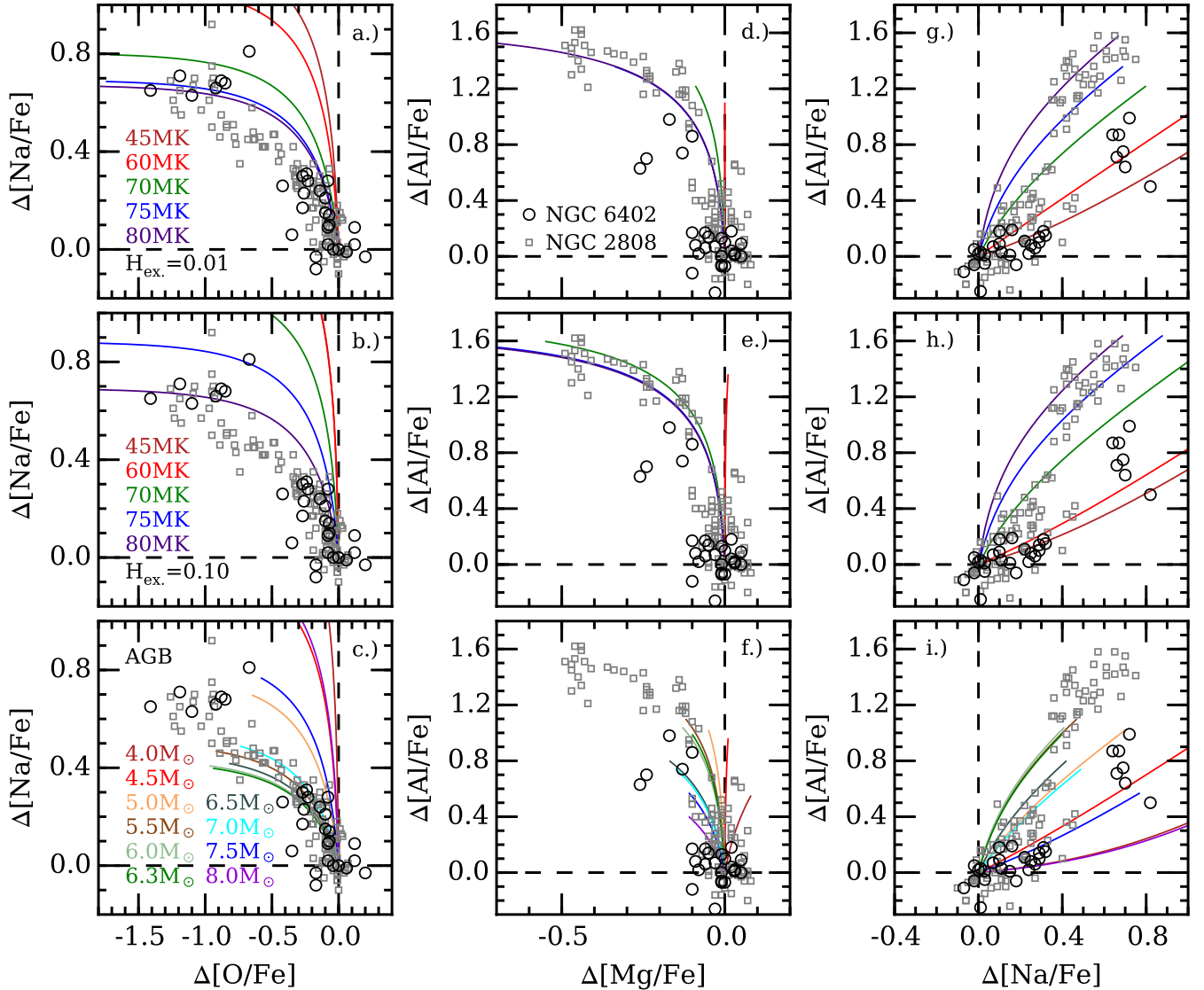


Figure 12. Similar to Fig. 11, the relative changes in the O-Na (panels a–c), Mg-Al (panels d–f), and Na-Al (panels g–i) (anti-)correlations are compared for NGC 6402 (large open circles) and NGC 2808 (small grey boxes). The top row (panels a, d, and g) overplots the composition changes and resulting dilution curves using data from Prantzos et al. (2007) when P1 gas is burned at various temperatures of 45–80 MK and reaches a hydrogen exhaustion (H_{ex} ; $(X_{\text{O}}-X)/X_{\text{O}}$) value of 0.01. The middle row (panels b, e, and h) are similar except the hydrogen exhaustion value is an order of magnitude higher at 0.10. The bottom row (panels c, f, and i) are similar except the different colored lines represent dilution curves based on the $Z = 10^{-3}$ AGB ejecta models of Ventura et al. (2013) for masses of 4–8 M_{\odot} . The key conclusions of this plot are: (1) Mg-depletion requires burning temperatures > 65 MK to explain the most extreme stars in both clusters; (2) no single dilution curve fits any cluster; (3) the E group in NGC 2808 may be understood as a result of hydrostatic burning at 75–80 MK, but the extreme stars in NGC 6402 seem to require ~ 70 MK conditions along with a higher ratio of pristine material to lower the [Na/Fe] and [Al/Fe] abundances; (4) the intermediate composition stars of NGC 2808 are fit by ~ 5.5 – $7 M_{\odot}$ AGB ejecta; and (5) the P2 stars of NGC 6402 are not fit by a single set of AGB yields, but may be compatible with ~ 7 – $8 M_{\odot}$ AGB ejecta if the [O/Fe] (for 7.5– $8 M_{\odot}$ models), [Na/Fe] (for 7.5– $8 M_{\odot}$ models), and/or [Al/Fe] (for $7 M_{\odot}$ models) yields can be reduced.

In Fig. 13, the most obvious difference between the two clusters is the paucity of red HB stars in NGC 6402. The red HB fraction for NGC 6402 is < 10 per cent (Contreras Peña et al. 2013) but exceeds 50 per cent for NGC 2808. Although some P1 stars may reside on the red HB in NGC 6402, the 10 per cent fraction is too low to account for the 34 per cent P1 ratio found here. Therefore, a large fraction of the P1 and P2 stars in NGC 6402 must be shifted to the RR Lyrae region and cool end of the blue HB sequence. In Fig. 13 this corresponds to the turn over

region near F439W–F555W ~ 0.5 mag., which leads us to conclude that the P1 and P2 stars in NGC 6402 reach the the zero age HB with lower envelope masses than their NGC 2808 counterparts. The exact reason for this discrepancy is not clear but could result if NGC 6402 stars lose mass on the RGB more efficiently, have higher *ab initio* He abundances (implying a shorter evolution time), or if NGC 6402 is considerably older.

Fig. 13 also highlights that the nearly vertical portions along the extended blue HBs also differ between the two

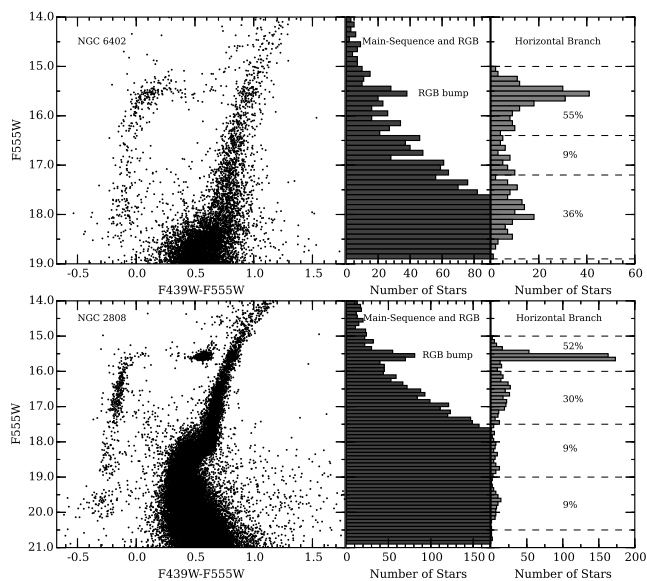


Figure 13. F555W versus F439W-F555W CMDs are shown for NGC 6402 (top) and NGC 2808 (bottom) using data from [Piotto et al. \(2002\)](#). Both clusters have similar metallicity and age values but exhibit very different horizontal branch morphologies. The luminosity functions to the right of each CMD are for the main-sequence and RGB populations (middle panels; dark grey) and horizontal branch (right panels; light grey) sequences.

clusters. For NGC 6402, 36 per cent of the HB stars belong to the extreme blue tail with only 9 per cent residing at intermediate luminosities. However, NGC 2808 has about 30 per cent of its stars at intermediate luminosities and only ~ 20 per cent on the extreme blue tail. For NGC 2808, the ratio of intermediate to extreme (plus blue hook) HB stars is roughly comparable to the I1+I2 and E population fractions given in [Carretta \(2015\)](#), respectively.

The combined observations indicate that at $[\text{Fe}/\text{H}] \sim -1.15$ the I1/I2 composition globular cluster stars scatter along the upper/middle portion of the blue HB in CMDs using the F439W and F555W filters while those of the E population reach the highest temperatures. The paucity of I1/I2 stars in NGC 6402 therefore seems a likely explanation for the small fraction of HB stars with $16 \lesssim F555W \lesssim 17$ mag. Furthermore, the comparatively high fraction of extreme blue HB stars in NGC 6402 suggests that the cluster was able to form an unusually large fraction of He-enhanced stars with minimal dilution.

Fig. 14 shows that the full HB morphology of NGC 6402 may be modeled relatively well using just two populations with different mean masses and He abundances but similar mass dispersions. We selected $Y = 0.3$ for the He-enhanced population since the zero-age HB locus fit the level of the brightest HB stars. However, we note that NGC 2808 may have ΔY values as high 0.13 (e.g., [Milone et al. 2015b](#)), and the combined HB and composition data suggest that NGC 6402 likely has $\Delta Y \sim 0.1$. This level of He enrichment could also fit the NGC 6402 HB as long as the most He-rich stars reside on the vertical portion of the blue HB.

Regardless of the exact ΔY value, the HB evolutionary tracks in Fig. 14 show that the most extreme blue HB stars will not evolve to ascend the AGB. As a result, we

expect that like several other clusters, including NGC 2808 ([Wang et al. 2016](#)), the AGB of NGC 6402 will be missing the most Na-rich stars. Differential reddening and field contamination make number counts of RGB and AGB stars in NGC 6402 difficult, but the cleaned CMD in Fig. 5 of [Contreras Peña et al. \(2018\)](#) suggests the AGB is sparsely populated.

5.5.1 NGC 2419 and NGC 6402

A comparison of the NGC 6402 CMD shown in Fig. 13 with the NGC 2419 CMD presented in Fig. 2 of [di Criscienzo et al. \(2011\)](#) reveals a striking similarity between the two clusters. The HBs of both clusters are numerically dominated by luminous blue HB stars and extreme blue HB stars, but each possesses a significant paucity of intermediate luminosity blue HB stars. In fact, the distributions of luminous blue HB, intermediate, and extreme HB stars are nearly identical with NGC 6402 having 55, 9, and 36 per cent ratios and NGC 2419 exhibiting 50, 9, and 41 per cent fractions, respectively ([Di Criscienzo et al. 2015](#)).

The similar HB distributions of NGC 6402 and NGC 2419 are particularly surprising given that the two clusters are separated in metallicity by about a factor of 10. Similar to the results presented here for NGC 6402, [Cohen & Kirby \(2012\)](#) and [Mucciarelli et al. \(2015\)](#) have also shown that NGC 2419 exhibits a strongly bimodal light element distribution with dominant populations of P1+P2 and E stars but a paucity of intermediate composition stars. Given suspicions that both NGC 6402 (e.g., [Contreras Peña et al. 2018](#)) and NGC 2419 (e.g., [Cohen & Kirby 2012](#)) may be the nuclear cores of former dwarf galaxies, it is possible that these clusters trace similar modes of star formation but at different metallicities. If true then similar clusters, both within and outside the Galaxy, may be identified by the existence of extended but strongly bimodal blue HB distributions.

5.6 NGC 6402 Chemical Composition Implications for Cluster Formation

As mentioned in Section 1, the detailed processes by which globular clusters form and undergo self-enrichment are unclear. Most models assume that so-called first generation stars are the first to form from the cluster’s natal gas (e.g., [D’Antona et al. 2016](#)). However, some models predict the opposite behavior and assume that the O/Mg-poor and N/Na/Al-rich stars form first ([Marcolini et al. 2009](#)). Establishing the order in which various globular cluster populations form would provide deep insight into the physical processes and pollution sources that shape the composition patterns observed today. In this context, the peculiar light element pattern of NGC 6402 may shed light on the cluster formation process.

Several lines of evidence indicate that P1 stars are the first to form. For example, Fig. 7 emphasizes that all old Galactic globular clusters examined to date have substantial populations of P1 stars. Fig. 7 also shows that lower mass clusters, which tend to exhibit smaller composition variations and therefore less self-enrichment, have the largest P1 fractions. We also note that clusters composed solely of intermediate or extreme composition stars have never been

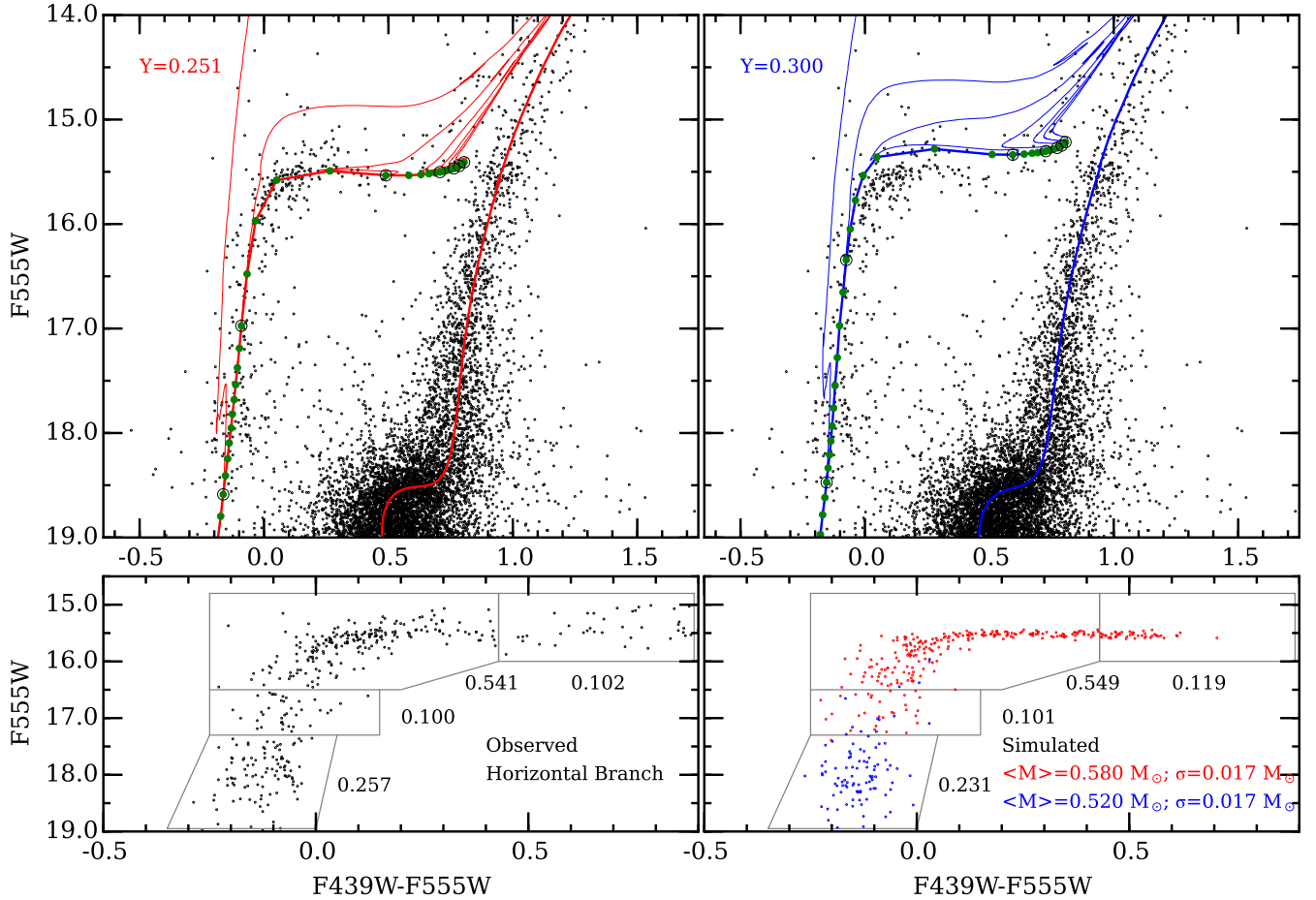


Figure 14. *Top:* F555W versus F439W-F555W CMDs are shown for NGC 6402 with 11.5 Gyr, α -enhanced, $[\text{Fe}/\text{H}] = -1$ BaSTI (Pietrinferni et al. 2004) isochrones and horizontal branch models shown for He abundances of $Y = 0.251$ (left panel; red) and $Y = 0.300$ (right panel; blue). The solid green circles on the zero-age horizontal branch represent masses ranging from about $0.8 M_{\odot}$ to $0.48 M_{\odot}$. The points with larger open black circles span, from blue to red, 0.5 to $0.8 M_{\odot}$ in $0.05 M_{\odot}$ increments. These points also have full evolutionary sequences drawn as light red and blue lines. *Bottom:* The left panel shows only the horizontal branch stars with the numerical values indicating fractional populations within each outlined region. The right panel shows a simulated horizontal branch assuming mean horizontal branch masses of $0.58 M_{\odot}$ ($\sigma = 0.017 M_{\odot}$) and $0.52 M_{\odot}$ ($\sigma = 0.017 M_{\odot}$) for the He-normal (first generation) and He-rich (second generation) stars, respectively. The simulations used the P1+P2 and E population ratios to determine the number of objects in the He-normal and He-rich groups.

found and that Rup 106, the only confirmed single population cluster (Villanova et al. 2013; Dotter et al. 2018), possesses solely low-Na stars. Additionally, a small number of N-rich stars, which may have originated in globular clusters, have been found in the Galactic bulge and halo (e.g., Martell et al. 2016; Schiavon et al. 2017), but the ratios are not high enough to suggest that clusters composed solely of “second generation” stars ever existed.

A more significant controversy surrounds the formation of the intermediate and extreme composition stars. Since most proposed pollution sources do not inherently produce the observed light element abundance patterns, models generally require some level of dilution between processed and pristine gas (e.g., D’Ercole et al. 2011; D’Antona et al. 2016). In fact, many models attempt to fit the light element distributions shown in Fig. 8 by mixing only P1 and E composition gas or P1 and model ejecta gas. Although these models produce reasonable fits for some clusters, recent analyses have shown that simple dilution models are

insufficient to simultaneously fit all of the populations in at least NGC 6752, NGC 2808, and NGC 5986 (Carretta et al. 2012, 2018; Johnson et al. 2017c). The inability of single dilution models to fit these clusters suggests that more than one pollution source was in operation (see also Section 5.4). In other words, intermediate and extreme globular cluster stars need not follow a common dilution function, form at the same time, nor originate from the same pollution source.

The large gaps in NGC 6402’s $[\text{O}/\text{Fe}]$, $[\text{Na}/\text{Fe}]$, and $[\text{Al}/\text{Fe}]$ abundances support the notion that most globular clusters are enriched by distinct, but separate, events rather than a simple dilution of single composition pristine and polluted gas. Since the I1/I2 stars are missing, or at least a minority population, in NGC 6402 but represent a large fraction of most clusters, the present data suggest that I1/I2 stars are the *last* group to form. Delayed formation of intermediate composition stars has been proposed in the past (e.g., Valcarce & Catelan 2011; D’Antona et al. 2016; Bekki et al. 2017; Kim & Lee 2018), but NGC 6402 repre-

sents the first direct evidence supporting such a hypothesis. The missing I1/I2 group further suggests that NGC 6402 may be a special case where star formation terminated prematurely.

If NGC 6402 is a preserved snapshot of globular cluster formation then the relationships between the P1, P2, and E populations are particularly intriguing. Fig. 7 shows that NGC 6402 has a large, but not unusual, number of P1 stars, and the available evidence is in-line with the previously stated assumption that these were among the first stars to form. In fact, the I1/I2 gap may completely rule out all formation scenarios where P1 stars form through any type of dilution event.

In Section 5.4, we used the different composition patterns of NGC 6402 and NGC 2808 to illustrate a fundamental disconnect between the formation of E and P2 population stars. Specifically, we concluded that the light element patterns of the two clusters could not be explained unless the P2 and E groups formed from gas that originated from different sources. The data therefore support a model in which E composition stars form as an independent group and where the P2, I1, and I2 stars are the only populations requiring significant dilution.

If AGB stars are important contributors of polluted gas, then the D’Ercole et al. (2008) model indicates that chemical enrichment via AGB winds could produce a cooling flow that funnels N/Na/Al-rich and O/Mg-poor gas toward the cluster core and result in the formation of intermediate composition stars, after mixing with pristine gas (see Fig. 15). The NGC 6402 data suggest that the P2 stars form before the I1 and I2 groups, which would invert the middle formation order presented by D’Antona et al. (2016). If P2 stars form before I1/I2 stars in all clusters then the data would indicate that a large reservoir of pristine gas must be present before the intermediate composition stars can start forming, which presumably occurs after the initial Type II supernova (SN) era. In this scenario, the I1/I2 composition stars would then form from gas experiencing a decreasing ratio of pristine-to-polluted material with time. However, the P2→I1→I2 sequence need not be universal since the I1/I2 stars could form before the P2 group if the polluting gas reaches a high enough density to initiate star formation before a substantial amount of pristine gas is re-accumulated after the SN era.

A delay of several tens of Myrs between the production of P1 and P2 stars seems required to provide enough time for the latter pollution source(s) (AGB stars?) to evolve. The “bubble” model described in D’Ercole et al. (2016) predicts a delay of > 40 Myr between the gas expulsion phase initiated by Type II supernovae (SNe) and the re-collapse/accretion of pristine material. Fig. 12 showed that AGB stars may be able to produce the P2, I1, and I2 composition stars, but the current models do not easily explain the E populations that are present in only the most massive clusters. Therefore, we hypothesize that the E stars require special circumstances for formation (see Fig. 15), and posit that both the P1 and E populations are formed very early in a cluster’s lifetime, perhaps within the first 5–10 Myr. We follow the hybrid pollution scenario presented in Sills & Glebbeek (2010) and suggest that supermassive star enrichment may provide a plausible explanation for the E population.

The formation of supermassive stars may be prominent

in the dense, gas-rich environments present in some early globular clusters, and Gieles et al. (2018) showed that the required conditions for these objects to form may be limited to the most massive clusters ($\gtrsim 10^6$ stars) with high gas accretion rates ($\gtrsim 10^5 M_{\odot} \text{ Myr}^{-1}$). With masses exceeding $10^3 M_{\odot}$, supermassive stars would be able to provide processed material to a cluster interstellar medium within the first few Myr, and Denissenkov & Hartwick (2014) showed that such stars could produce gas matching the composition of E stars. The high He and N abundances of the E composition gas would permit efficient cooling (Herwig et al. 2012) and further favor rapid and early star formation. Additional He and N enhancements could also be provided from the winds of massive WN type Wolf-Rayet stars and Luminous Blue Variables as well (e.g., Dufour et al. 1997; Smith & Morse 2004; Smith 2006). Gieles et al. (2018) also noted that winds from a central supermassive star may be confined within a small “stall radius”, where the wind pressure and ambient cluster pressure are equal, which could maintain an environment that largely excluded mixing with pristine gas and promoted the formation of nearly pure E composition stars (see Fig. 15). Since lower mass clusters would not form supermassive stars, the production of E group stars would be limited to the most massive clusters with the highest gas accretion rates. Furthermore, confinement of the supermassive star winds to small cluster radii would provide a natural explanation for the frequently observed central concentration of E composition stars (e.g., Carretta et al. 2010b; Johnson & Pilachowski 2010; Lardo et al. 2011; Johnson & Pilachowski 2012).

Regardless of the specific mechanism that produces E composition stars, kinematic studies support the notion that the E populations represent distinct formation events. In addition to being preferentially located near the cores of several clusters, the E stars can also exhibit faster rotation (Cordero et al. 2017) and possibly smaller line-of-sight velocity dispersions (e.g., Bellazzini et al. 2012; Kučinskas et al. 2014; Cordero et al. 2017) than other cluster sub-populations. In this light NGC 6402 is no exception since the velocity dispersions for the P1, P2, P1+P2, and E populations are 11.4, 8.0, 9.5, and 4.6 km s^{-1} , respectively. However, the number of targets and radial sampling in the present data set are too small to draw any firm conclusions regarding kinematic and/or radial distribution signatures that may be unique to the E population in NGC 6402.

The scenario outlined in Fig. 15 indicates that the E and I2 groups are both composed of nearly pure polluted material except that each would originate from a different source. Although direct comparisons between E and I2 stars are sparse in the literature, we note that Li observations may provide some support of different origins for the E and I2 groups. If intermediate and extreme composition stars formed from gas burned at high temperatures then lithium’s low destruction temperature ($\sim 2.5 \times 10^6$ K) means A(Li) should strongly decrease in intermediate and extreme stars. Li should also be anti-correlated with elements such as Na and Al, but D’Orazi et al. (2015) found that Li abundances are generally invariant as a function of [Na,Al/Fe]. On the other hand, Lind et al. (2009), D’Orazi et al. (2015), and Mucciarelli et al. (2018) have shown that E composition

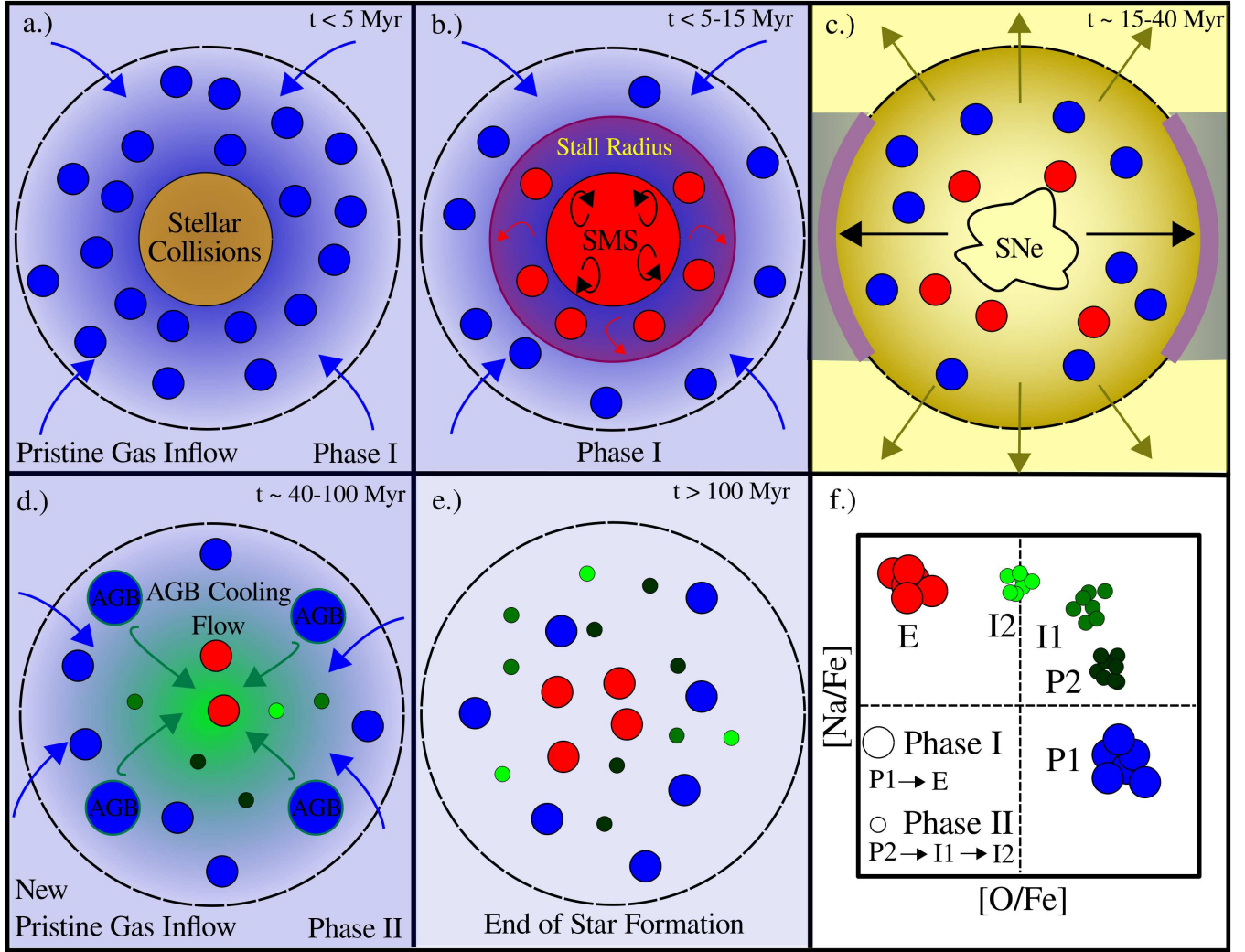


Figure 15. An illustration of the proposed globular cluster formation model. Note that the schematic is not to scale. Panel (a) illustrates the formation of P1 first generation stars (blue filled circles) from the initial cold gas present in the cluster. P1 stars are assumed to form at all radii and follow a typical cluster density profile. For sufficiently massive and dense cluster cores, stellar collisions are likely to occur and result in the production of a centrally concentrated supermassive star (SMS; $\gtrsim 10^3 M_{\odot}$). Following [Gieles et al. \(2018\)](#) and [Denissenkov & Hartwick \(2014\)](#), panel (b) indicates that the fully convective SMS will eject gas that has been processed at high temperatures and matches the composition of E stars (red filled circles). [Gieles et al. \(2018\)](#) predict that the SMS gas will be retained within a central “stall radius” (where the SMS wind pressure matches the intracluster gas pressure) and lead to the formation of E composition stars. After ~ 10 – 15 Myr, panel (c) illustrates that the first Type II SNe will explode and drive out the intracluster gas, which may also coincide with the dissolution of the SMS. Following the [D’Ercole et al. \(2016\)](#) bubble model, a cluster forming within a dense disk may eject most of its gas out of the plane but retain some local gas in a shell within the plane (thick purple lines). Panel (d) indicates that after the SN era is over the cluster will accumulate more pristine gas and also develop a central cooling flow of intermediate mass AGB ejecta. Mixing of pristine and AGB gas will produce the P2, I1, and I2 intermediate composition stars (small filled green circles). The formation order will depend on the local ratio of pristine-to-polluted gas, but the results from NGC 6402 indicate that the P2 stars can form first. Panel (e) shows the cluster composition after star formation has ceased, and panel (f) is a schematic illustration of the $[O/Fe]$ and $[Na/Fe]$ abundances for each population.

stars in particular are Li-depleted, which follows the hypothesis that the P2, I1, and I2 groups in globular clusters are polluted by different sources (where some Li may have been produced) than the E stars. We note that some authors do find Li-Na anti-correlations that are not restricted to just the E populations (e.g., [Pasquini et al. 2005](#); [Bonifacio et al. 2007](#)) so it is possible that the production (or not) of Li is cluster specific and depends on the particular polluting source(s) mixing with pristine gas.

The model shown in Fig. 15 attempts to alleviate many

of the cluster formation problems outlined in Fig. 6 of [Bastian & Lardo \(2018\)](#), particularly with regard to detailed abundance patterns, the discrete nature of various sub-populations, and relationships between composition variations and cluster mass. On the other hand, the mass budget problem may persist and the present model still requires a full enrichment timescale of at least 40–100 Myr, which seems to contrast with observations of many nearby young massive clusters that appear to become gas free after only a few Myr (e.g., [Bastian et al. 2014](#); [Hollyhead et al.](#)

2015). The lack of an Fe spread in clusters that continued to form stars after the SN era could also be a concern. However, we note that the products of SN explosions are not guaranteed to contaminate the intracluster gas (e.g., Tenorio-Tagle et al. 2015) nor completely clear a cluster of natal gas (e.g., D’Ercole et al. 2016).

It is possible that many of the investigated young massive clusters are not actually close analogs of early globular clusters, and/or that the early Universe environment favored higher gas densities than are common today (e.g., Elmegreen 2017; Pfeffer et al. 2018). Interestingly, the “supernebula” region located in NGC 5253 may provide an alternative analog to early globular cluster formation as it contains at least two compact, young ($\sim 1\text{--}3$ Myr), deeply embedded, and massive ($\sim 2 \times 10^6 M_{\odot}$ combined) star clusters with star formation efficiencies of $\sim 30\text{--}70$ per cent (e.g., Beck et al. 1996; Calzetti et al. 2015; Turner et al. 2015, 2017; Miura et al. 2018). This region also contains several thousand O stars, many Wolf-Rayet stars, perhaps a dozen or more very massive stars exceeding $150 M_{\odot}$, and may also have a top-heavy initial mass function (e.g., Turner et al. 2015, 2017). The extremely high densities experienced by the supernebula may be driven in part by the infall of a diffuse HI cloud (López-Sánchez et al. 2012; Westmoquette et al. 2013), and it is possible that this environment somewhat resembles early globular cluster formation occurring during the dominant galaxy assembly and star formation epoch at high redshift.

Although the supernebula clusters are still embedded in their natal clouds, several analyses have detected N-enhanced gas, along with an anti-correlation between $\log(\text{O}/\text{H})$ and $\log(\text{N}/\text{O})$, associated with the supernebula region that could be connected to pollution from Wolf-Rayet stars, Luminous Blue Variable stars, and/or very massive ($> 100 M_{\odot}$) stars (Walsh & Roy 1987; Kobulnicky et al. 1997; López-Sánchez et al. 2007; Monreal-Ibero et al. 2010; Westmoquette et al. 2013; Smith et al. 2016). He enhancements have also been detected (López-Sánchez et al. 2007) but are so far unconfirmed (Monreal-Ibero et al. 2013). Cohen et al. (2018) showed that strong radiative cooling within the NGC 5253 supernebula region is likely stalling stellar winds and preventing the formation of significant cluster-scale outflow, which could enable prolonged star formation from chemically enriched gas. Even if the pollution sources are not exactly the same as those in early Universe massive clusters, the results from NGC 5253 indicate that enriched gas from massive stars can be produced quickly and retained for at least a few Myr within an extremely dense proto-cluster region¹⁰. Furthermore, Silich & Tenorio-Tagle

(2017) showed that massive compact clusters, such as those within the NGC 5253 supernebula, will likely retain some natal gas through the SN era. This mode of gas retention supports the possibility of a delayed star formation epoch featuring pollution from longer lived sources, such as AGB stars (see also Kim & Lee 2018).

To summarize (see also Fig. 15), we hypothesize that monometallic globular clusters form in two distinct stages. During phase one, which likely occurs during the first few Myr, all globular clusters form P1 composition stars at a variety of radii. In the most massive systems with the highest gas accretion rates, central supermassive stars form via runaway collisions (e.g., Sills & Glebbeek 2010; Gieles et al. 2018) and pollute cluster cores with the products of high temperature proton-capture burning¹¹. Strong radiative cooling and the stalling of stellar winds promote rapid star formation, significant gas retention, and inhibit the mixing of polluted and pristine gas, which produces a centrally concentrated population of E composition stars. Following the model presented by D’Ercole et al. (2016), core-collapse SNe halt star formation for $\sim 15\text{--}40$ Myr until enough pristine gas can be accumulated to start the second, delayed formation phase. After ~ 40 Myr, the D’Antona et al. (2016) model indicates that $< 8 M_{\odot}$ AGB stars can start contributing processed gas and mixing with pristine material. The I1/I2 gap in NGC 6402 suggests that stars with the highest pristine-to-polluted gas ratios form first (P2 group), and that the I1 and I2 populations form later as the pristine gas fraction drops. Presumably, star formation is permanently halted either by the mechanical ejection of all gas (e.g., Type Ia SNe) or when the remaining gas density falls below a critical limit.

6 SUMMARY

This paper presents radial velocity and/or chemical abundance measurements for 41 RGB stars in the massive Galactic globular cluster NGC 6402 using data obtained with the M2FS instrument in high resolution mode. We find a mean cluster heliocentric radial velocity of -61.1 km s^{-1} with a dispersion of 8.5 km s^{-1} . Additionally, we measured $\langle [\text{Fe}/\text{H}] \rangle = -1.13$ dex and a small star-to-star dispersion of 0.05 dex.

The overall composition properties of NGC 6402 are similar to those of other inner Galaxy clusters such that NGC 6402 is generally α -enhanced, has approximately solar $[\text{Cr}, \text{Ni}/\text{Fe}]$ ratios, and exhibits a moderately low $\langle [\text{La}/\text{Eu}] \rangle = -0.08$ dex. None of the elements heavier than Ca show any evidence supporting significant abundance spreads.

The light elements O, Na, Mg, Al, and Si exhibit clear

¹⁰ We note that if the winds from Wolf-Rayet stars, Luminous Blue Variables, and other massive stars are enriched almost exclusively in He/N then these sources may explain the suspected He/N-enhanced first generation stars noted by Milone et al. (2018) and Lardo et al. (2018). Following Silich & Tenorio-Tagle (2017), the retention (or not) of early ejecta from high mass stars may be strongly tied to the mass and density of the proto-cluster environment, which is at least qualitatively in agreement with the observed correlation between present-day cluster mass and the estimated He-spread among first generation stars shown in Milone et al. (2018, their Figure 19). The strong density requirement for retaining stellar winds shown by Silich & Tenorio-Tagle

(2017, their Figure 1), especially at high star formation efficiency, may explain why only some clusters with similar masses exhibit He/N spreads among their first generation populations (Milone et al. 2018; Lardo et al. 2018).

¹¹ The proposed cluster formation model does not necessarily require a central $> 10^3 M_{\odot}$ star, especially since such supermassive stars have never been observed. Instead, the only requirements are that a mechanism exists to produce very O/Mg-poor and He/Na/Al-rich gas on a time scale $\lesssim 10$ Myr, that this process favors dense, high cluster mass environments, and that most of the material is confined to the cluster core.

(anti-)correlations that follow the typical patterns observed in other massive Galactic clusters. We also found some evidence supporting a correlation between $[\text{Al}/\text{Fe}]$ and $[\text{Ca}/\text{Fe}]$, but a comparison with NGC 2808 suggests that the Al-Ca correlation may be spurious. Interestingly, the $[\text{O}/\text{Fe}]$, $[\text{Na}/\text{Fe}]$, and $[\text{Al}/\text{Fe}]$ data exhibit large abundance gaps that indicate a missing or minority population of intermediate composition stars.

Statistical analyses and an examination of NGC 6402's HB morphology suggest that intermediate composition stars likely represent < 10 per cent of the total cluster population. However, the extreme composition stars constitute > 25 per cent of our sample, and their likely location on the high temperature tail of the blue HB may correlate with a high He abundance as well.

A detailed light element composition comparison between NGC 6402 and NGC 2808 indicates that the various sub-populations in NGC 6402 formed from gas that was burned at different temperatures. This result suggests that in NGC 6402, and probably most clusters, the full extension of light element abundance variations is likely driven by pollution from multiple sources. In agreement with some theoretical models, the observed $[\text{O}/\text{Fe}]$, $[\text{Na}/\text{Fe}]$, and $[\text{Al}/\text{Fe}]$ gaps in NGC 6402 seem to indicate that intermediate composition stars are the last group to form. As a result, we followed previous work to develop a qualitative formation model in which monometallic globular clusters experience two distinct phases of star formation.

In the first rapid formation stage, a significant fraction of pristine gas is converted into stars that exhibit “halo-like” abundance patterns. During this first formation phase, high mass clusters such as NGC 6402 may also be able to drive the production of supermassive stars near their cores, and as a result produce centrally concentrated populations of extreme composition stars. Recent examinations of young massive clusters indicate that they may become gas free after only ~ 5 – 10 Myr, and we posit that the most extreme composition stars in globular clusters probably form within this approximate time frame. Rapid star formation may be further aided by the enhanced He and N abundances of E composition gas, which has been shown to permit efficient cooling. An examination of the supernova region in NGC 5253 suggests that rapid chemical enrichment is possible within very dense proto-cluster cores, and wind stalling may further promote prolonged star formation from chemically enriched gas. Following the notation of Carretta (2015), clusters like NGC 6402 would contain mostly P1 and E stars at the end of the first formation stage. In contrast, lower mass clusters would not be able to form central supermassive stars and as a result would only have P1 composition stars at the end of the first formation phase. In both cases, star formation would likely cease for ~ 10 – 40 Myr while core-collapse SNe explode and drive out gas.

After ~ 40 Myr, a second star formation event is initialized when the re-accumulated gas density reaches some critical value. Although present-day young massive clusters do not seem to retain natal gas after 40 Myr, Silich & Tenorio-Tagle (2017) showed that gas retention is possible for very compact proto-clusters. A combination of polluted gas, perhaps driven by various cluster sources such as intermediate mass AGB stars, and pristine gas would then mix to produce the variety of intermediate composition stars

found in nearly all globular clusters. The time scale of gas accumulation and the rate at which the pristine-to-polluted gas ratio changes would then govern the exact distribution of intermediate composition stars, which would likely vary from cluster-to-cluster. For NGC 6402, the missing I1/I2 populations suggest that P2 stars can form first during this later phase. Since P2 stars have high pristine-to-polluted gas ratios, the NGC 6402 data indicate that the delayed star formation phase is dependent on the re-accumulation of pristine gas for initialization. In this case, the process of forming P2→I1→I2 stars would make sense if the cluster's overall ratio of pristine-to-polluted gas decreased with time. For all clusters, star formation would cease when the gas density became too low or was otherwise removed (e.g., Type Ia SNe). In the case of NGC 6402, the small or missing I1 and I2 groups suggest that star formation was prematurely halted and that the cluster may represent a frozen snap shot of the chemical enrichment process.

ACKNOWLEDGEMENTS

This research has made use of NASA's Astrophysics Data System Bibliographic Services. This publication has made use of data products from the Two Micron All Sky Survey, which is a joint project of the University of Massachusetts and the Infrared Processing and Analysis Center/California Institute of Technology, funded by the National Aeronautics and Space Administration and the National Science Foundation. We thank Jean Turner for helpful discussions related to NGC 5253. C.I.J. gratefully acknowledges support from the Clay Fellowship, administered by the Smithsonian Astrophysical Observatory.

REFERENCES

- Bastian N., Lardo C., 2018, *ARA&A*, **56**, 83
 Bastian N., Lamers H. J. G. L. M., de Mink S. E., Longmore S. N., Goodwin S. P., Gieles M., 2013, *MNRAS*, **436**, 2398
 Bastian N., Hollyhead K., Cabrera-Ziri I., 2014, *MNRAS*, **445**, 378
 Bastian N., Cabrera-Ziri I., Salaris M., 2015, *MNRAS*, **449**, 3333
 Baumgardt H., Hilker M., 2018, *MNRAS*, **478**, 1520
 Beck S. C., Turner J. L., Ho P. T. P., Lacy J. H., Kelly D. M., 1996, *ApJ*, **457**, 610
 Bekki K., Jeřábková T., Kroupa P., 2017, *MNRAS*, **471**, 2242
 Bellazzini M., Bragaglia A., Carretta E., Gratton R. G., Lucatello S., Catanzaro G., Leone F., 2012, *A&A*, **538**, A18
 Bensby T., et al., 2017, *A&A*, **605**, A89
 Boehm-Vitense E., 1979, *ApJ*, **234**, 521
 Bond H. E., 1975, *ApJ*, **202**, L47
 Bonifacio P., et al., 2007, *A&A*, **470**, 153
 Breen P. G., 2018, *MNRAS*, **481**, L110
 Buzzoni A., Patelli L., Bellazzini M., Pecci F. F., Oliva E., 2010, *MNRAS*, **403**, 1592
 Calzetti D., et al., 2015, *ApJ*, **811**, 75
 Cannon R. D., Niss B., Norgaard-Nielsen H. U., 1981, *MNRAS*, **196**, 1P
 Carretta E., 2015, *ApJ*, **810**, 148
 Carretta E., Bragaglia A., 2018, *A&A*, **614**, A109
 Carretta E., Recio-Blanco A., Gratton R. G., Piotto G., Bragaglia A., 2007, *ApJ*, **671**, L125
 Carretta E., et al., 2009a, *A&A*, **505**, 117

- Carretta E., Bragaglia A., Gratton R., Lucatello S., 2009b, *A&A*, **505**, 139
- Carretta E., Bragaglia A., Gratton R. G., Recio-Blanco A., Lucatello S., D'Orazi V., Cassisi S., 2010a, *A&A*, **516**, A55
- Carretta E., Bragaglia A., D'Orazi V., Lucatello S., Gratton R. G., 2010b, *A&A*, **519**, A71
- Carretta E., et al., 2010c, *A&A*, **520**, A95
- Carretta E., Bragaglia A., Gratton R. G., Lucatello S., D'Orazi V., 2012, *ApJ*, **750**, L14
- Carretta E., et al., 2014, *A&A*, **564**, A60
- Carretta E., Bragaglia A., Lucatello S., Gratton R. G., D'Orazi V., Sollima A., 2018, *A&A*, **615**, A17
- Castelli F., Kurucz R. L., 2004, ArXiv Astrophysics e-prints, Catelan M., 2009, *Ap&SS*, **320**, 261
- Cohen J. G., Kirby E. N., 2012, *ApJ*, **760**, 86
- Cohen D. P., Turner J. L., Consiglio S. M., Martin E. C., Beck S. C., 2018, *ApJ*, **860**, 47
- Contreras Peña C., Catelan M., Grundahl F., Stephens A. W., Smith H. A., 2013, *AJ*, **146**, 57
- Contreras Peña C., Catelan M., Grundahl F., Stephens A. W., Smith H. A., 2018, *AJ*, **155**, 116
- Cordero M. J., Hénault-Brunet V., Pilachowski C. A., Balbinot E., Johnson C. I., Varri A. L., 2017, *MNRAS*, **465**, 3515
- Côté P., Hanes D. A., McLaughlin D. E., Bridges T. J., Hesser J. E., Harris G. L. H., 1997, *ApJ*, **476**, L15
- Cunha K., Smith V. V., Bergemann M., Suntzeff N. B., Lambert D. L., 2010, *ApJ*, **717**, 333
- D'Antona F., Ventura P., 2007, *MNRAS*, **379**, 1431
- D'Antona F., Caloi V., Montalbán J., Ventura P., Gratton R., 2002, *A&A*, **395**, 69
- D'Antona F., Vesperini E., D'Ercole A., Ventura P., Milone A. P., Marino A. F., Tailo M., 2016, *MNRAS*, **458**, 2122
- D'Ercole A., Vesperini E., D'Antona F., McMillan S. L. W., Recchi S., 2008, *MNRAS*, **391**, 825
- D'Ercole A., D'Antona F., Vesperini E., 2011, *MNRAS*, **415**, 1304
- D'Ercole A., D'Antona F., Vesperini E., 2016, *MNRAS*, **461**, 4088
- D'Orazi V., et al., 2015, *MNRAS*, **449**, 4038
- Da Costa G. S., 2016, in Bragaglia A., Arnaboldi M., Rejkuba M., Romano D., eds, IAU Symposium Vol. 317, The General Assembly of Galaxy Halos: Structure, Origin and Evolution. pp 110–115 ([arXiv:1510.00873](https://arxiv.org/abs/1510.00873)), doi:10.1017/S174392131500678X
- Da Costa G. S., Norris J. E., Yong D., 2013, *ApJ*, **769**, 8
- Decressin T., Charbonnel C., Meynet G., 2007, *A&A*, **475**, 859
- Denisenkov P. A., Denisenkova S. N., 1990, *Soviet Astronomy Letters*, **16**, 275
- Denissenkov P. A., Hartwick F. D. A., 2014, *MNRAS*, **437**, L21
- Denissenkov P. A., VandenBerg D. A., Hartwick F. D. A., Herwig F., Weiss A., Paxton B., 2015, *MNRAS*, **448**, 3314
- Di Criscienzo M., Tailo M., Milone A. P., D'Antona F., Ventura P., Dotter A., Brocato E., 2015, *MNRAS*, **446**, 1469
- Di Criscienzo M., Ventura P., D'Antona F., Dell'Agli F., Tailo M., 2018, *MNRAS*, **479**, 5325
- Dickens R. J., 1972, *MNRAS*, **159**, 7P
- Dotter A., Milone A. P., Conroy C., Marino A. F., Sarajedini A., 2018, *ApJ*, **865**, L10
- Dufour R. J., Glover T. W., Hester J. J., Curie D. G., van Orsow D., Walter D. K., 1997, in Nota A., Lamers H., eds, Astronomical Society of the Pacific Conference Series Vol. 120, Luminous Blue Variables: Massive Stars in Transition. p. 255
- Elmegreen B. G., 2017, *ApJ*, **836**, 80
- Gao S., Jiang B.-W., Zhao Y.-H., 2007, *Chinese J. Astron. Astrophys.*, **7**, 111
- Gieles M., et al., 2018, *MNRAS*, **478**, 2461
- González Hernández J. I., Bonifacio P., 2009, *A&A*, **497**, 497
- Gratton R. G., et al., 2001, *A&A*, **369**, 87
- Gratton R., Sneden C., Carretta E., 2004, *ARA&A*, **42**, 385
- Gratton R. G., et al., 2007, *A&A*, **464**, 953
- Gratton R. G., Carretta E., Bragaglia A., Lucatello S., D'Orazi V., 2010, *A&A*, **517**, A81
- Gratton R. G., Lucatello S., Carretta E., Bragaglia A., D'Orazi V., Momany Y. A., 2011, *A&A*, **534**, A123
- Gratton R. G., et al., 2013, *A&A*, **549**, A41
- Gratton R. G., et al., 2014, *A&A*, **563**, A13
- Gratton R. G., et al., 2015, *A&A*, **573**, A92
- Harding G. A., 1962, *The Observatory*, **82**, 205
- Herwig F., VandenBerg D. A., Navarro J. F., Ferguson J., Paxton B., 2012, *ApJ*, **757**, 132
- Hesser J. E., Shawl S. J., Meyer J. E., 1986, *PASP*, **98**, 403
- Hollyhead K., Bastian N., Adamo A., Silva-Villa E., Dale J., Ryon J. E., Gazak Z., 2015, *MNRAS*, **449**, 1106
- Iliadis C., Karakas A. I., Prantzos N., Lattanzio J. C., Doherty C. L., 2016, *ApJ*, **818**, 98
- Johnson C. I., Pilachowski C. A., 2010, *ApJ*, **722**, 1373
- Johnson C. I., Pilachowski C. A., 2012, *ApJ*, **754**, L38
- Johnson C. I., Pilachowski C. A., Michael Rich R., Fulbright J. P., 2009, *ApJ*, **698**, 2048
- Johnson C. I., Rich R. M., Kobayashi C., Kunder A., Koch A., 2014, *AJ*, **148**, 67
- Johnson C. I., Rich R. M., Pilachowski C. A., Caldwell N., Mateo M., Bailey III J. I., Crane J. D., 2015, *AJ*, **150**, 63
- Johnson C. I., Caldwell N., Rich R. M., Walker M. G., 2017a, *AJ*, **154**, 155
- Johnson C. I., Caldwell N., Rich R. M., Mateo M., Bailey III J. I., Clarkson W. I., Olszewski E. W., Walker M. G., 2017b, *ApJ*, **836**, 168
- Johnson C. I., Caldwell N., Rich R. M., Mateo M., Bailey III J. I., Olszewski E. W., Walker M. G., 2017c, *ApJ*, **842**, 24
- Johnson C. I., Rich R. M., Caldwell N., Mateo M., Bailey III J. I., Olszewski E. W., Walker M. G., 2018, *AJ*, **155**, 71
- Karakas A. I., Lattanzio J. C., 2003, *Publ. Astron. Soc. Australia*, **20**, 279
- Karakas A. I., Marino A. F., Nataf D. M., 2014, *ApJ*, **784**, 32
- Kim J. J., Lee Y.-W., 2018, *ApJ*, **869**, 35
- Kimmig B., Seth A., Ivans I. I., Strader J., Caldwell N., Anderton T., Gregersen D., 2015, *AJ*, **149**, 53
- Kobulnicky H. A., Skillman E. D., Roy J.-R., Walsh J. R., Rosa M. R., 1997, *ApJ*, **477**, 679
- Kraft R. P., 1994, *PASP*, **106**, 553
- Krause M., Charbonnel C., Decressin T., Meynet G., Prantzos N., 2013, *A&A*, **552**, A121
- Kurtz M. J., Mink D. J., 1998, *PASP*, **110**, 934
- Kučinskas A., Dobrovolskas V., Bonifacio P., 2014, *A&A*, **568**, L4
- Langer G. E., Hoffman R., Sneden C., 1993, *PASP*, **105**, 301
- Lapenna E., Mucciarelli A., Ferraro F. R., Origlia L., Lanzoni B., Massari D., Dalessandro E., 2015, *ApJ*, **813**, 97
- Lardo C., Bellazzini M., Pancino E., Carretta E., Bragaglia A., Dalessandro E., 2011, *A&A*, **525**, A114
- Lardo C., Mucciarelli A., Bastian N., 2016, *MNRAS*, **457**, 51
- Lardo C., Salaris M., Bastian N., Mucciarelli A., Dalessandro E., Cabrera-Ziri I., 2018, *A&A*, **616**, A168
- Lawler J. E., Bonvallet G., Sneden C., 2001a, *ApJ*, **556**, 452
- Lawler J. E., Wickliffe M. E., den Hartog E. A., Sneden C., 2001b, *ApJ*, **563**, 1075
- Lee Y.-W., Gim H. B., Casetti-Dinescu D. I., 2007, *ApJ*, **661**, L49
- Lind K., Primas F., Charbonnel C., Grundahl F., Asplund M., 2009, *A&A*, **503**, 545
- López-Sánchez Á. R., Esteban C., García-Rojas J., Peimbert M., Rodríguez M., 2007, *ApJ*, **656**, 168
- López-Sánchez Á. R., Koribalski B. S., van Eymeren J., Esteban C., Kirby E., Jerjen H., Lonsdale N., 2012, *MNRAS*, **419**, 1051
- Maccarone T. J., Zurek D. R., 2012, *MNRAS*, **423**, 2
- Marcolini A., Gibson B. K., Karakas A. I., Sánchez-Blázquez P., 2009, *MNRAS*, **395**, 719
- Marino A. F., Villanova S., Piotto G., Milone A. P., Momany Y., Bedin L. R., Medling A. M., 2008, *A&A*, **490**, 625

- Marino A. F., et al., 2011a, *A&A*, **532**, A8
- Marino A. F., Villanova S., Milone A. P., Piotto G., Lind K., Geisler D., Stetson P. B., 2011b, *ApJ*, **730**, L16
- Marino A. F., et al., 2011c, *ApJ*, **731**, 64
- Marino A. F., et al., 2014, *MNRAS*, **437**, 1609
- Marino A. F., et al., 2017, *ApJ*, **843**, 66
- Marino A. F., et al., 2018, *ApJ*, **859**, 81
- Martell S. L., et al., 2016, *ApJ*, **825**, 146
- Mateo M., Bailey J. I., Crane J., Shtetman S., Thompson I., Roederer I., Bigelow B., Gunnels S., 2012, in *Ground-based and Airborne Instrumentation for Astronomy IV*. p. 84464Y, doi:10.1117/12.926448
- Milone A. P., et al., 2014, *ApJ*, **785**, 21
- Milone A. P., et al., 2015a, *MNRAS*, **447**, 927
- Milone A. P., et al., 2015b, *ApJ*, **808**, 51
- Milone A. P., et al., 2017, *MNRAS*, **464**, 3636
- Milone A. P., et al., 2018, *MNRAS*, **481**, 5098
- Miura R. E., Espada D., Hirota A., Nakanishi K., Bendo G. J., Sugai H., 2018, *ApJ*, **864**, 120
- Monreal-Ibero A., Vilchez J. M., Walsh J. R., Muñoz-Tuñón C., 2010, *A&A*, **517**, A27
- Monreal-Ibero A., Walsh J. R., Westmoquette M. S., Vilchez J. M., 2013, *A&A*, **553**, A57
- Mucciarelli A., Bellazzini M., Ibata R., Merle T., Chapman S. C., Dalessandro E., Sollima A., 2012, *MNRAS*, **426**, 2889
- Mucciarelli A., Bellazzini M., Merle T., Plez B., Dalessandro E., Ibata R., 2015, *ApJ*, **801**, 68
- Mucciarelli A., Merle T., Bellazzini M., 2017, *A&A*, **600**, A104
- Mucciarelli A., Salaris M., Monaco L., Bonifacio P., Fu X., Villanova S., 2018, *A&A*, **618**, A134
- Nataf D. M., Gould A. P., Pinsonneault M. H., Udalski A., 2013, *ApJ*, **766**, 77
- Pasquini L., Bonifacio P., Molaro P., Francois P., Spite F., Gratton R. G., Carretta E., Wolff B., 2005, *A&A*, **441**, 549
- Pfeffer J., Kruijssen J. M. D., Crain R. A., Bastian N., 2018, *MNRAS*, **475**, 4309
- Pietrinferni A., Cassisi S., Salaris M., Castelli F., 2004, *ApJ*, **612**, 168
- Piotto G., et al., 2002, *A&A*, **391**, 945
- Piotto G., et al., 2005, *ApJ*, **621**, 777
- Piotto G., et al., 2015, *AJ*, **149**, 91
- Prantzos N., Charbonnel C., Iliadis C., 2007, *A&A*, **470**, 179
- Prantzos N., Charbonnel C., Iliadis C., 2017, *A&A*, **608**, A28
- Renzini A., et al., 2015, *MNRAS*, **454**, 4197
- Salinas R., Strader J., 2015, *ApJ*, **809**, 169
- Schiavon R. P., et al., 2017, *MNRAS*, **465**, 501
- Sharina M., Aringer B., Davoust E., Kniazev A. Y., Donzelli C. J., 2012, *MNRAS*, **426**, L31
- Shetrone M. D., 1996, *AJ*, **112**, 2639
- Silich S., Tenorio-Tagle G., 2017, *MNRAS*, **465**, 1375
- Sills A., Glebbeek E., 2010, *MNRAS*, **407**, 277
- Skrutskie M. F., et al., 2006, *AJ*, **131**, 1163
- Smith G. H., 2006, *PASP*, **118**, 1225
- Smith N., Morse J. A., 2004, *ApJ*, **605**, 854
- Smith L. J., Crowther P. A., Calzetti D., Sidoli F., 2016, *ApJ*, **823**, 38
- Snedden C., 1973, *ApJ*, **184**, 839
- Snedden C., Kraft R. P., Guhathakurta P., Peterson R. C., Fulbright J. P., 2004, *AJ*, **127**, 2162
- Tailo M., et al., 2017, *MNRAS*, **465**, 1046
- Tenorio-Tagle G., Muñoz-Tuñón C., Silich S., Cassisi S., 2015, *ApJ*, **814**, L8
- Turner J. L., Beck S. C., Benford D. J., Consiglio S. M., Ho P. T. P., Kovács A., Meier D. S., Zhao J.-H., 2015, *Nature*, **519**, 331
- Turner J. L., Consiglio S. M., Beck S. C., Goss W. M., Ho P. T. P., Meier D. S., Silich S., Zhao J.-H., 2017, *ApJ*, **846**, 73
- Valcarce A. A. R., Catelan M., 2011, *A&A*, **533**, A120
- Ventura P., D'Antona F., 2009, *A&A*, **499**, 835
- Ventura P., D'Antona F., Di Criscienzo M., Carini R., D'Ercole A., vesperini E., 2012, *ApJ*, **761**, L30
- Ventura P., Di Criscienzo M., Carini R., D'Antona F., 2013, *MNRAS*, **431**, 3642
- Ventura P., D'Antona F., Imbriani G., Di Criscienzo M., Dell'Agli F., Tailo M., 2018, *MNRAS*, **477**, 438
- Villanova S., Geisler D., 2011, *A&A*, **535**, A31
- Villanova S., Geisler D., Carraro G., Moni Bidin C., Muñoz C., 2013, *ApJ*, **778**, 186
- Walsh J. R., Roy J.-R., 1987, *ApJ*, **319**, L57
- Wang Y., Primas F., Charbonnel C., Van der Swaelmen M., Bono G., Chantreau W., Zhao G., 2016, *A&A*, **592**, A66
- Webbink R. F., 1981, *ApJS*, **45**, 259
- Westmoquette M. S., James B., Monreal-Ibero A., Walsh J. R., 2013, *A&A*, **550**, A88
- Yong D., Grundahl F., Lambert D. L., Nissen P. E., Shetrone M. D., 2003, *A&A*, **402**, 985
- Yong D., et al., 2014a, *MNRAS*, **439**, 2638
- Yong D., et al., 2014b, *MNRAS*, **441**, 3396
- de Mink S. E., Pols O. R., Langer N., Izzard R. G., 2009, *A&A*, **507**, L1
- di Criscienzo M., et al., 2011, *MNRAS*, **414**, 3381

Table 1. Table 1: star identifiers, sky coordinates, photometry, radial velocities, and model atmosphere parameters are provided for all member and non-member stars observed for this program.

Star Name (2MASS)	RA (J2000)	DEC (J2000)	J (mag.)	H (mag.)	K _S (mag.)	RV _{Helio.} (km s ⁻¹)	RV Error (km s ⁻¹)	T _{eff} (K)	log(g) (cgs)	[Fe/H] (dex)	ξ _{mic.} (km s ⁻¹)
Cluster Members											
2M17372576–0314077	264.357353	–3.235491	11.368	10.505	10.246	–64.3	0.5	4175	1.00	–1.13	1.90
2M17372832–0314210	264.368037	–3.239184	11.732	10.850	10.643	–63.4	0.7
2M17373006–0314502	264.375283	–3.247291	11.640	10.848	10.545	–50.2	0.4
2M17373048–0315530	264.377033	–3.264747	10.967	10.106	9.856	–60.5	2.0
2M17373178–0313592	264.382423	–3.233112	12.188	11.382	11.167	–58.7	0.6	4425	1.40	–1.14	1.65
2M17373225–0311152	264.384408	–3.187576	10.966	10.071	9.817	–56.9	0.5	4075	0.85	–1.13	1.95
2M17373243–0313213	264.385131	–3.222595	12.209	11.394	11.175	–64.1	0.9	4375	1.25	–1.14	1.65
2M17373305–0311386	264.387709	–3.194075	11.951	11.185	10.947	–63.3	0.5	4375	1.20	–1.14	1.75
2M17373325–0315382	264.388560	–3.260634	10.987	10.040	9.772	–63.7	0.4	4075	1.05	–1.15	1.95
2M17373336–0315103	264.389006	–3.252870	12.057	11.234	10.965	–60.0	0.5	4300	1.00	–1.09	1.55
2M17373351–0314396	264.389637	–3.244342	10.951	10.014	9.753	–66.0	0.6	4035	0.60	–1.17	1.85
2M17373366–0312495	264.390260	–3.213775	12.227	11.401	11.210	–45.5	0.3	4425	1.40	–1.11	1.70
2M17373382–0315285	264.390933	–3.257925	12.310	11.470	11.268	–61.7	0.7	4475	1.50	–1.17	1.70
2M17373390–0313291	264.391283	–3.224769	10.983	10.043	9.774	–73.0	0.8	4065	0.45	–1.21	1.95
2M17373395–0313138	264.391472	–3.220503	11.803	10.918	10.710	–68.1	0.6	4375	1.25	–1.10	1.85
2M17373458–0315552	264.394097	–3.265336	12.087	11.258	11.036	–59.1	0.2	4500	1.60	–1.13	1.75
2M17373460–0314057	264.394192	–3.234935	11.614	10.716	10.533	–43.7	0.4	4275	1.05	–1.18	1.60
2M17373470–0315094	264.394601	–3.252625	11.579	10.750	10.503	–62.2	0.5
2M17373606–0315251	264.400256	–3.256982	10.957	10.032	9.785	–50.3	0.2	4300	1.15	–1.22	1.75
2M17373691–0313304	264.403825	–3.225115	11.637	10.796	10.529	–59.2	0.4	4315	1.10	–1.11	1.85
2M17373796–0314120	264.408198	–3.236675	11.311	10.434	10.152	–73.7	0.8	4125	1.00	–1.21	1.80
2M17373815–0314496	264.408965	–3.247136	11.726	10.899	10.629	–68.2	0.9	4350	1.35	–1.15	1.80
2M17373864–0313445	264.411013	–3.229044	10.897	9.991	9.708	–64.7	0.4	4075	0.60	–1.25	1.80
2M17373909–0313237	264.412881	–3.223258	12.128	11.286	11.079	–77.7	1.3
2M17373921–0314264	264.413402	–3.240683	11.042	10.166	9.879	–54.0	0.1	4175	0.90	–1.18	1.85
2M17373944–0314480	264.414374	–3.246685	12.308	11.478	11.274	–71.8	1.2	4475	1.55	–1.13	1.60
2M17373961–0315269	264.415077	–3.257477	10.903	9.975	9.725	–53.0	0.2	4200	1.05	–1.17	2.05
2M17374031–0315544	264.417992	–3.265132	10.895	9.983	9.713	–68.6	0.8	4150	0.95	–1.17	1.95
2M17374053–0314592	264.418885	–3.249801	12.039	11.247	11.011	–62.8	0.7	4400	1.15	–1.17	1.60
2M17374093–0315327	264.420575	–3.259104	10.904	9.991	9.728	–46.0	0.1	4150	0.65	–1.01	1.75
2M17374103–0313167	264.420999	–3.221331	11.852	11.038	10.782	–59.4	0.2	4475	1.65	–1.14	1.85
2M17374139–0313528	264.422492	–3.231334	12.354	11.530	11.274	–65.7	0.8
2M17374163–0314213	264.423482	–3.239265	11.337	10.385	10.148	–58.1	0.4	4075	0.75	–1.06	1.75
2M17374212–0315069	264.425504	–3.251931	11.846	11.110	10.743	–70.6	1.2	4375	1.45	–1.11	1.70
2M17374273–0315238	264.428065	–3.256630	11.403	10.504	10.288	–60.7	0.3	4300	1.25	–1.09	1.90
2M17374309–0314044	264.429546	–3.234561	10.920	10.006	9.778	–44.9	0.2	4150	1.00	–1.16	1.90
2M17374421–0313013	264.434233	–3.217049	11.873	10.993	10.771	–55.4	0.2	4350	1.35	–1.01	1.75
2M17374450–0314255	264.435418	–3.240421	11.985	11.133	10.906	–57.1	0.3	4350	1.35	–1.12	1.85
2M17374518–0314040	264.438288	–3.234462	11.854	10.997	10.780	–66.7	0.8	4275	1.10	–1.13	1.70
2M17374581–0314407	264.440914	–3.244651	11.441	10.578	10.318	–77.8	1.0	4250	1.35	–1.02	1.80
2M17374610–0315079	264.442089	–3.252207	11.378	10.480	10.246	–55.1	0.5	4250	1.10	–1.13	1.85
Non-Members											
2M17372950–0314302	264.372934	–3.241728	11.834	11.041	10.782	–7.7	1.0

Table 2. Table 2: abundance ratios and population designations for all member stars.

Star (2MASS)	Population	[FeI/H] (dex)	[FeII/H] (dex)	[OI/Fe] (dex)	[NaI/Fe] (dex)	[MgI/Fe] (dex)	[AlI/Fe] (dex)	[SiI/Fe] (dex)	[CaI/Fe] (dex)	[CrI/Fe] (dex)	[NiI/Fe] (dex)	[LaII/Fe] (dex)	[EuII/Fe] (dex)
2M17372576–0314077	P2	-1.12	-1.13	0.60	0.05	0.42	0.59	0.27	0.27	0.17	-0.07	0.35	0.21
2M17372832–0314210
2M17373006–0314502
2M17373048–0315530
2M17373178–0313592	P1	-1.12	-1.15	0.53	-0.13	0.39	0.34	0.31	0.27	-0.03	-0.07	0.28	0.23
2M17373225–0311152	E	-1.13	-1.13	-0.22	0.56	0.30	1.27	0.63	0.31	0.04	-0.15	0.16	0.42
2M17373243–0313213	P2	-1.13	-1.15	0.28	0.16	...	0.46	0.34	0.38	0.08	-0.19	0.11	0.39
2M17373305–0311386	P2	-1.14	-1.14	...	0.31	0.41	0.57	0.35	0.41	0.02	-0.10	0.28	0.32
2M17373325–0315382	P1	-1.14	-1.16	0.62	-0.08	0.39	0.35	0.47	0.10	0.07	-0.10	0.45	0.53
2M17373336–0315103	E	-1.09	-1.09	-0.71	0.55	0.16	1.11	0.37	0.39	0.08	-0.21
2M17373351–0314396	E	-1.16	-1.17	-0.49	0.61	0.23	1.39	0.45	0.35	0.02	-0.10	0.34	0.38
2M17373366–0312495	P2	-1.11	-1.11	0.44	0.13	0.43	0.42	0.28	0.29	0.04	-0.09	0.40	0.41
2M17373382–0315285	E	-1.17	-1.17	-0.18	0.59	0.14	1.04	0.40	0.37	0.11	-0.08	0.22	0.42
2M17373390–0313291	P2	-1.23	-1.19	0.47	0.18	0.45	0.50	0.33	0.29	0.02	-0.17	0.23	0.31
2M17373395–0313138	P2	-1.10	...	0.56	0.14	0.37	0.48	0.38	0.41	0.16	-0.11	0.39	0.35
2M17373458–0315552	P2	-1.13	-1.13	0.63	0.04	0.45	0.41	0.22	0.33	0.11	-0.06	0.30	0.38
2M17373460–0314057	P1	-1.17	-1.18	0.62	-0.01	0.34	0.58	0.38	0.35	0.05	0.00	0.30	0.31
2M17373470–0315094
2M17373606–0315251	P1	-1.21	-1.22	0.76	-0.11	0.43	0.42	0.21	0.30	0.14	-0.12	0.32	0.60
2M17373691–0313304	E	-1.10	-1.11	-0.40	0.53	...	1.27	0.35	0.42	0.13	-0.06	0.33	0.36
2M17373796–0314120	P1	-1.20	-1.21	0.90	-0.13	0.42	0.45	0.34	0.26	0.00	-0.11	0.28	0.39
2M17373815–0314496	E	-1.15	-1.15	-0.15	0.58	0.27	1.15	0.36	0.37	0.21	-0.03	0.42	0.40
2M17373864–0313445	P2	-1.25	-1.25	0.60	0.11	0.40	0.51	0.34	0.32	0.14	-0.04	0.25	0.40
2M17373909–0313237
2M17373921–0314264	P1	-1.20	-1.16	0.70	-0.10	0.37	0.15	0.29	0.29	-0.01	-0.17	0.20	0.27
2M17373944–0314480	P1	-1.12	-1.14	...	0.00	0.44	0.37	0.17	0.25	-0.04	-0.11	0.30	0.28
2M17373961–0315269	P1	-1.17	-1.17	0.82	-0.08	0.39	0.41	0.32	0.30	0.17	-0.05	0.32	0.52
2M17374031–0315544	P2	-1.17	-1.17	0.62	0.18	0.39	0.54	0.31	0.34	0.24	-0.08	0.33	0.40
2M17374053–0314592	P2	-1.17	-1.17	0.35	-0.04	0.34	0.47	0.30	0.21	0.03	-0.24	0.24	...
2M17374093–0315327	P1	-1.01	-1.01	0.53	-0.18	0.30	0.29	0.17	0.31	0.05	-0.19	0.13	0.26
2M17374103–0313167	P2	-1.13	-1.14	...	0.21	0.40	0.38	0.32	0.42	0.12	0.00	0.39	0.49
2M17374139–0313528
2M17374163–0314213	E	-1.05	-1.06	0.03	0.71	...	0.90	0.66	0.33	0.06	-0.10	0.18	0.31
2M17374212–0315069	P1	-1.09	-1.13	0.82	-0.01	0.31	0.49	0.27	0.30	0.11	-0.15	0.40	0.46
2M17374273–0315238	P2	-1.08	-1.10	0.43	0.20	0.30	0.58	0.35	0.35	0.13	-0.13	0.29	0.35
2M17374309–0314044	P2	-1.15	-1.16	0.46	0.21	0.35	0.55	0.21	0.29	0.07	-0.16	0.31	0.41
2M17374421–0313013	E	-1.01	-1.01	...	0.51	0.03	1.26	0.41	0.29	0.00	-0.23	0.35	0.31
2M17374450–0314255	P1	-1.11	-1.12	0.66	-0.10	0.43	0.43	0.37	0.25	-0.02	-0.10	0.39	0.28
2M17374518–0314040	E	-1.12	-1.13	-0.13	...	0.26	1.06	0.32	0.38	0.04	-0.14	0.25	0.28
2M17374581–0314407	P1	-1.00	-1.03	0.63	0.00	0.32	0.43	0.28	0.28	0.02	-0.13	0.39	0.52
2M17374610–0315079	P2	-1.13	-1.12	0.43	0.07	0.40	0.34	0.45	0.23	-0.04	-0.15	0.20	0.36

Table 3. Table 3: abundance ratio uncertainties for all member stars.

Star (2MASS)	$\Delta[\text{FeI}/\text{H}]$ (dex)	$\Delta[\text{FeII}/\text{H}]$ (dex)	$\Delta[\text{OI}/\text{Fe}]$ (dex)	$\Delta[\text{NaI}/\text{Fe}]$ (dex)	$\Delta[\text{MgI}/\text{Fe}]$ (dex)	$\Delta[\text{AlI}/\text{Fe}]$ (dex)	$\Delta[\text{SiI}/\text{Fe}]$ (dex)	$\Delta[\text{CaI}/\text{Fe}]$ (dex)	$\Delta[\text{CrI}/\text{Fe}]$ (dex)	$\Delta[\text{NiI}/\text{Fe}]$ (dex)	$\Delta[\text{LaII}/\text{Fe}]$ (dex)	$\Delta[\text{EuII}/\text{Fe}]$ (dex)
2M17372576–0314077	0.10	0.12	0.10	0.08	0.07	0.08	0.07	0.07	0.09	0.05	0.13	0.11
2M17372832–0314210
2M17373006–0314502
2M17373048–0315530
2M17373178–0313592	0.10	0.14	0.10	0.06	0.07	0.08	0.08	0.07	0.07	0.09	0.13	0.11
2M17373225–0311152	0.10	0.12	0.10	0.11	0.07	0.07	0.10	0.06	0.08	0.05	0.13	0.11
2M17373243–0313213	0.10	0.14	0.10	0.05	...	0.08	0.07	0.05	0.10	0.12	0.13	0.11
2M17373305–0311386	0.10	0.13	...	0.17	0.07	0.07	0.12	0.08	0.09	0.07	0.13	0.11
2M17373325–0315382	0.10	0.11	0.10	0.08	0.07	0.08	0.07	0.09	0.07	0.07	0.13	0.11
2M17373336–0315103	0.10	0.12	0.10	0.05	0.07	0.16	0.10	0.06	0.10	0.08
2M17373351–0314396	0.10	0.12	0.10	0.08	0.07	0.08	0.10	0.05	0.12	0.07	0.13	0.11
2M17373366–0312495	0.10	0.13	0.10	0.06	0.07	0.09	0.08	0.06	0.07	0.07	0.13	0.11
2M17373382–0315285	0.10	0.17	0.10	0.08	0.07	0.11	0.08	0.06	0.09	0.07	0.13	0.11
2M17373390–0313291	0.10	0.12	0.10	0.07	0.07	0.07	0.07	0.06	0.07	0.06	0.13	0.11
2M17373395–0313138	0.10	...	0.10	0.06	0.07	0.09	0.07	0.07	0.08	0.07	0.13	0.11
2M17373458–0315552	0.10	0.13	0.10	0.07	0.07	0.08	0.07	0.06	0.07	0.07	0.13	0.11
2M17373460–0314057	0.10	0.11	0.10	0.05	0.07	0.08	0.07	0.07	0.07	0.06	0.13	0.11
2M17373470–0315094
2M17373606–0315251	0.10	0.12	0.10	0.05	0.07	0.14	0.08	0.05	0.09	0.07	0.13	0.11
2M17373691–0313304	0.10	...	0.10	0.05	...	0.08	0.09	0.07	0.08	0.08	0.13	0.11
2M17373796–0314120	0.10	0.12	0.10	0.05	0.07	0.08	0.07	0.08	0.07	0.05	0.13	0.11
2M17373815–0314496	0.10	0.12	0.10	0.07	0.07	0.07	0.07	0.07	0.07	0.06	0.13	0.11
2M17373864–0313445	0.10	0.12	0.10	0.11	0.07	0.08	0.07	0.08	0.07	0.06	0.13	0.11
2M17373909–0313237
2M17373921–0314264	0.10	0.14	0.10	0.05	0.07	0.07	0.12	0.07	0.09	0.07	0.13	0.11
2M17373944–0314480	0.10	0.11	...	0.09	0.07	0.08	0.07	0.08	0.09	0.06	0.13	0.11
2M17373961–0315269	0.10	0.14	0.10	0.07	0.07	0.11	0.09	0.07	0.12	0.06	0.13	0.11
2M17374031–0315544	0.10	0.12	0.10	0.05	0.07	0.10	0.07	0.08	0.07	0.06	0.13	0.11
2M17374053–0314592	0.10	0.12	0.10	0.07	0.07	0.08	0.08	0.08	0.08	0.06	0.13	0.11
2M17374093–0315327	0.10	0.11	0.10	0.06	0.07	0.07	0.09	0.06	0.08	0.07	0.13	0.11
2M17374103–0313167	0.10	0.12	...	0.07	0.07	0.08	0.10	0.12	0.10	0.08	0.13	0.11
2M17374139–0313528
2M17374163–0314213	0.10	0.11	0.10	0.06	0.07	0.07	0.07	0.06	0.12	0.12	0.13	0.11
2M17374212–0315069	0.10	0.12	0.10	0.06	0.07	0.07	0.09	0.07	0.11	0.05	0.13	0.11
2M17374273–0315238	0.10	0.13	0.10	0.07	0.07	0.07	0.08	0.07	0.09	0.06	0.13	0.11
2M17374309–0314044	0.10	0.13	0.10	0.05	0.07	0.13	0.07	0.05	0.13	0.06	0.13	0.11
2M17374421–0313013	0.10	0.12	...	0.06	0.07	0.07	0.10	0.09	0.10	0.06	0.13	0.11
2M17374450–0314255	0.10	0.12	0.10	0.06	0.07	0.08	0.07	0.08	0.08	0.08	0.13	0.11
2M17374518–0314040	0.10	0.12	0.10	...	0.07	0.08	0.07	0.06	0.11	0.09	0.13	0.11
2M17374581–0314407	0.10	0.11	0.10	0.06	0.07	0.07	0.10	0.06	0.08	0.06	0.13	0.11
2M17374610–0315079	0.10	0.12	0.10	0.08	0.07	0.07	0.10	0.08	0.09	0.08	0.13	0.11

Table 4. Table 4: mean abundance ratios and Welch's t -test results for the P1, P2, and E populations.

Mean Abundance Ratios											
Population	[Fe/H]	[O/Fe]	[Na/Fe]	[Mg/Fe]	[Al/Fe]	[Si/Fe]	[Ca/Fe]	[Cr/Fe]	[Ni/Fe]	[La/Fe]	[Eu/Fe]
...	(dex)	(dex)	(dex)	(dex)	(dex)	(dex)	(dex)	(dex)	(dex)	(dex)	(dex)
P1	-1.13	0.69	-0.08	0.38	0.39	0.30	0.27	0.04	-0.11	0.31	0.39
P2	-1.15	0.49	0.14	0.39	0.49	0.32	0.32	0.09	-0.11	0.29	0.37
E	-1.11	-0.28	0.58	0.20	1.16	0.44	0.36	0.08	-0.12	0.28	0.36
t -statistics, degrees of freedom, and p-values											
t (P1-P2)	0.50	4.09	-7.40	-0.83	-2.50	-0.64	-2.11	-1.76	0.23	0.67	0.47
d.o.f	18	20	23	22	20	19	24	24	24	23	16
p-value	0.62	5.50×10^{-4}	1.68×10^{-7}	0.42	0.02	0.53	0.05	0.09	0.82	0.51	0.65
t (P1-E)	-0.89	10.62	-23.66	4.65	-13.03	-2.91	-3.81	-1.16	0.52	0.77	0.65
d.o.f	19	10	15	8	14	14	19	18	15	15	16
p-value	0.38	1.17×10^{-6}	3.54×10^{-13}	1.65×10^{-3}	3.92×10^{-9}	0.01	1.19×10^{-3}	0.26	0.62	0.45	0.53
t (P2-E)	-1.64	8.58	-13.69	5.16	-12.43	-2.74	-1.45	0.53	0.31	0.24	0.29
d.o.f	15	9	19	7	11	11	21	19	17	13	17
p-value	0.12	1.14×10^{-5}	2.68×10^{-11}	1.10×10^{-3}	1.01×10^{-7}	0.02	0.16	0.61	0.76	0.81	0.78

This paper has been typeset from a $\text{\TeX}/\text{\LaTeX}$ file prepared by the author.